



24 silicon at core-mantle boundary conditions. Comparing our new equation of state to that of iron  
25 and the density of the core, we find that for an Fe-Ni-Si outer core,  $11.3 \pm 1.5$  wt% silicon would  
26 be required to match the core's observed density at the core-mantle boundary. We have also  
27 performed first-principles calculations of the equations of state of Fe<sub>3</sub>Si with the D0<sub>3</sub> structure,  
28 hcp iron, and FeSi with the B2 structure using density-functional theory.

29

30 Keywords: Earth's core, equation of state, phase diagram, iron alloys

31

32

### 33 **1. Introduction**

34

35 The Earth's core is comprised mostly of iron, with some nickel, and several weight  
36 percent of one or more light elements (Birch, 1952). Candidates for this light element component  
37 include silicon, oxygen, sulfur, carbon, and hydrogen (e.g. McDonough, 2003). There is  
38 evidence that silicon is present in the core to at least some degree, and it may be the dominant  
39 light element. For example, silicon is known to partition into iron under reducing conditions, it is  
40 found in the metal of some enstatite chondrites, and silicon in the core is permitted by  
41 comparisons of Mg/Si and Fe/Si ratios between the Earth and chondrites (Allègre et al., 1995;  
42 McDonough, 2003). Silicon partitioning into the core may explain the difference between  
43 <sup>30</sup>Si/<sup>28</sup>Si ratios in terrestrial rocks versus meteorites (Fitoussi et al., 2009; Georg et al., 2007;  
44 Shahar et al., 2009). Experimental studies have demonstrated the ability of silicon to partition  
45 into liquid iron metal at high pressures (e.g. Knittle and Jeanloz, 1991; Ozawa et al., 2009;  
46 Takafuji et al., 2005), though this may require very reducing conditions (Malavergne et al.,

47 2004). Estimates of the maximum silicon content of the core vary widely, from ~6-7 wt%  
48 (Allègre et al., 1995; Javoy et al., 2010; McDonough, 2003; Shahar et al., 2009) to 8-11 wt%  
49 (Lin et al., 2003; Ricolleau et al., 2011) to up to 20 wt% (Balchan and Cowan, 1966; Ringwood,  
50 1959), if silicon is the dominant light element.

51         If silicon is a primary light element component in the core, its impact on the density of  
52 iron-rich melts is vital to interpretation of the composition, dynamics, and evolution of the core.  
53 Knowledge of its melting curve and phase relations can be used to constrain the thermal structure  
54 of the core and crystal structure of the inner core. Therefore, it is critical to understand the high  
55 pressure, high temperature phase relations, melting curve, and thermodynamics of the Fe-Si  
56 system. In this study, we focus on the equations of state and phase diagram of Fe-16wt%Si  
57 (hereafter Fe-16Si). This information can be compared to the Preliminary Reference Earth Model  
58 (PREM), a seismologically determined model of the Earth's density structure (Dziewonski and  
59 Anderson, 1981), to evaluate its importance as a core component. The composition we  
60 investigated is within the range expected for the Earth's core, but its high  $P$ - $T$  phase diagram has  
61 not been established. Additionally, thermal equations of state of iron-silicon alloys to high  
62 pressures have not been the subject of any recent studies. By determining the equation of state of  
63 Fe-16Si, the results from this study will allow us to constrain the amount of silicon needed to  
64 match the core density deficit.

65         Fe-16Si is close to stoichiometric  $\text{Fe}_3\text{Si}$ , or suessite (Keil et al., 1982). Alloys with  
66 similar compositions have been the subjects of several previous studies using varying methods.  
67 Yu and Secco (2008) investigated the equation of state of liquid alloy containing 17 wt% Si to 12  
68 GPa using the sink/float technique, while Lin et al. (2003) and Hirao et al. (2004) performed static  
69 compression on solid Fe-17Si and Fe-18Si, respectively, at room temperature. Zhang and Guyot

70 (1999) studied Fe-17Si in a large volume press. Asanuma et al. (2010) measured the melting  
71 curve of Fe-18Si to 119 GPa, and Morard et al. (2011) determined the melting curve of Fe-5Ni-  
72 15Si to 80 GPa. Moroni et al. (1999) calculated an equation of state of Fe<sub>3</sub>Si using density-  
73 functional calculations based on ultrasoft pseudopotentials and all-electron methods. Fe<sub>3</sub>Si was  
74 predicted to have the D0<sub>3</sub> (Strukturbericht designation), or BiF<sub>3</sub>-type, crystal structure at ambient  
75 conditions using LSDA methods (Christensen et al., 2008; Rhee, 2004). The one bar lattice  
76 parameter of Fe<sub>3</sub>Si has been predicted by Christensen et al. (2008) and Rhee (2004), and  
77 measured by Mishra et al. (1985). The one bar phase diagram in the Fe-FeSi system at high  
78 temperatures was reported by Massalski (1986). Kuwayama and Hirose (2004) studied phase  
79 relations in the Fe-FeSi system at 21 GPa, finding a eutectic point at 26 wt% Si and ~2100 K.  
80 Detailed theoretical analyses of the same system were performed by Zhang and Oganov (2010)  
81 and Côté et al. (2008), suggesting that silicon may stabilize the bcc structure in iron.

82         In this study, we determine the subsolidus phase diagram of Fe-16Si at high pressures  
83 and temperatures using synchrotron X-ray diffraction in a laser-heated diamond anvil cell. We  
84 measure its melting curve by looking for diffuse scattering in the diffraction patterns, and  
85 determine which phase is stable on the liquidus. We also determine the equations of state of all  
86 phases up to pressures of the Earth's outer core, by measuring the volumes of our samples under  
87 pressure by X-ray diffraction or calculating sample volumes using density functional theory.  
88 This allows for calculation of the amount of silicon required to match the observed core density  
89 deficit.

90

91

92 **2. Methods**

93

94           The starting material was Fe-Si alloy containing 15.9 wt% silicon ( $\text{Fe}_{0.73}\text{Si}_{0.27}$  by mole),  
95 based on electron microprobe measurements performed at the University of Maryland, and was  
96 found to be chemically homogeneous (Miller, 2009). The material was obtained from Keokuk  
97 Electro-Metals Company. The powder, with initial grain size  $\sim 5\text{-}20\ \mu\text{m}$ , was pressed in a  
98 diamond anvil cell to form a foil approximately  $3\text{-}5\ \mu\text{m}$  thick. Gaskets, initially  $250\ \mu\text{m}$  thick,  
99 were made of rhenium or stainless steel and were preindented to  $\sim 27\ \text{GPa}$  or  $\sim 18\ \text{GPa}$ ,  
100 respectively. A hole  $50\text{-}120\ \mu\text{m}$  in diameter was drilled in the center of the indentation to form  
101 the sample chamber. Diamond anvils used had  $300$  or  $400\ \mu\text{m}$  culets, or they were beveled, with  
102  $120$ ,  $150$ , or  $250\ \mu\text{m}$  flats and an  $8^\circ$  bevel out to  $300\ \mu\text{m}$ . For high temperature experiments, the  
103 sample was loaded between two layers of KBr  $\sim 10\ \mu\text{m}$  thick, which served as the pressure  
104 medium, pressure standard, and thermal insulator (Campbell et al., in prep). The sample  
105 assembly was oven-dried at  $85^\circ\text{C}$  for approximately one hour prior to compression. For  $300\ \text{K}$   
106 experiments, the sample was loaded as a loose powder with a few grains of KBr and ruby to  
107 serve as pressure standards (Campbell et al., in prep; Mao et al., 1986), then neon was loaded  
108 into the sample chamber as a pressurized gas to serve as the hydrostatic pressure medium using  
109 the COMPRES/GSECARS gas-loading system at the Advanced Photon Source (APS), Argonne  
110 National Laboratory (Rivers et al., 2008).

111           Laser-heating experiments were performed with angle-dispersive X-ray diffraction at  
112 beamline 13-ID-D (GeoSoilEnviroCARS) of the APS (Prakapenka et al., 2008; Shen et al.,  
113 2005). Room temperature experiments were performed with angle-dispersive X-ray diffraction at  
114 beamline 12.2.2 of the Advanced Light Source (ALS), Lawrence Berkeley National Laboratory  
115 (Kunz et al., 2005), and beamline X17C of the National Synchrotron Light Source (NSLS),

116 Brookhaven National Laboratory (Hu et al., 2006). Incident X-ray beams were monochromatic,  
117 and sample-to-detector distances were calibrated by 1 bar diffraction of CeO<sub>2</sub> (APS and NSLS)  
118 or LaB<sub>6</sub> (ALS). At the APS,  $\lambda=0.3344 \text{ \AA}$ , and the incident X-ray beam measured  $\sim 3 \text{ \mu m} \times 4 \text{ \mu m}$   
119 (FWHM). Diffracted X-rays were recorded using a MAR165 detector, with typical exposure  
120 times of 5 seconds. At the ALS,  $\lambda=0.41323 \text{ \AA}$ , and a MAR345 image plate or Bruker CCD  
121 detector was used. The incident beam measured  $30 \text{ \mu m} \times 30 \text{ \mu m}$ , and exposures were typically 20  
122 seconds. At the NSLS,  $\lambda=0.37677 \text{ \AA}$ , and the incident beam was  $26 \text{ \mu m} \times 25 \text{ \mu m}$ . A Fuji image  
123 plate was used, with typical exposure times of 5 minutes.

124         The X-ray diffraction patterns were integrated to produce 2 $\theta$  plots using Fit2D  
125 (Hammersley et al., 1996). Peak fitting of the integrated patterns was performed using PeakFit  
126 (Systat Software). Overlapping peaks were resolved in nearly all cases, and were not used in  
127 lattice parameter calculations if they could not be separated. Pressures were determined from the  
128 volume of B2-KBr, using the thermal equation of state of Campbell et al. (in prep). The equation  
129 of state parameters for KBr used in this study are listed in Table 1. This equation of state  
130 calibrates KBr against platinum, gold, hcp-iron, and MgO at room temperature and during laser  
131 heating, up to pressures of  $>100 \text{ GPa}$ . When calibrating the equation of state at high  
132 temperatures, KBr served as the thermal insulator, as in the present study. To measure the  
133 pressure in this study, the lattice parameter of KBr, and its uncertainty, was determined as the  
134 average and standard error from four to thirteen  $d$ -spacings. Uncertainties in pressure were  
135 propagated through the KBr equation of state from the uncertainty in temperature and the  
136 uncertainty in the lattice parameter. In the room temperature experiments, ruby fluorescence and  
137 the lattice parameter of neon served as secondary pressure standards (Dewaele et al., 2008; Mao  
138 et al., 1986).

139           The temperature of the KBr insulator/calibrant in our experiments was not the same as  
140 the sample temperature, because of axial gradients through the insulating layer. The KBr  
141 temperature was corrected downward from the measured temperature to  $T_{\text{KBr}} = (3T_{\text{meas}} + 300)/4$   
142  $\pm (T_{\text{meas}} - 300)/4$  (Campbell et al., 2009). The resulting error in pressure due to this large  
143 uncertainty in the temperature of the KBr is typically only a few percent, because the  
144 compressibility of KBr is high relative to its thermal expansion (Campbell et al., 2009, in prep).  
145 In using KBr as the pressure standard, we are assuming mechanical equilibrium between the  
146 sample and the pressure medium. Deviatoric stresses on the sample are expected to be negligible  
147 at high temperatures, compared to our experimental uncertainties.

148           The sample was compressed to a target pressure and laser-heated from each side by 1.064  
149  $\mu\text{m}$  Yb fiber lasers with ‘flat top’ profiles created by pi-shaping optics, with the laser power on  
150 each side being independently adjustable (Prakapenka et al., 2008). The diamond cells were  
151 water-cooled during heating. The temperature was slowly stepped up by increasing the laser  
152 power on both sides until a target temperature was reached, and then the laser power was  
153 gradually decreased to zero, with diffraction patterns being obtained on both heating and cooling  
154 cycles. Temperatures were determined spectroradiometrically (Heinz and Jeanloz, 1987) using  
155 the graybody approximation, and were measured during the collection of each diffraction pattern.  
156 The laser-heated spots were 20-25  $\mu\text{m}$  in diameter, much larger than the X-ray beam to minimize  
157 radial temperature gradients, and were coaligned with the beam using X-ray induced  
158 fluorescence from the KBr pressure medium. Temperatures were measured both upstream and  
159 downstream of the sample from a region 5  $\mu\text{m}$  in diameter in the center of the laser-heated spot,  
160 comparable to the size of the area probed by the X-rays.

161           Temperatures measured on the upstream and downstream sides of the sample were

162 averaged to obtain the sample temperature. For subsolidus phase diagram and equation of state  
163 measurements, the temperatures were then corrected downward by 3% to account for an axial  
164 temperature gradient through the thickness of the sample (Campbell et al., 2007, 2009). Reported  
165 uncertainties in the temperature incorporate an analytical uncertainty of 100 K from the  
166 temperature measurement system (Shen et al., 2001), the difference between the upstream and  
167 downstream temperatures (typically less than 100 K), and the uncertainty from the correction for  
168 the axial temperature gradient (Campbell et al., 2007, 2009), if applicable.

169         To benchmark the temperature measurements, a sample of pure iron loaded in an MgO  
170 pressure medium was analyzed using the methods outlined above to check the location of the  
171 hcp-fcc phase transition in iron, after Fischer et al. (2011). The sample was pressurized and laser-  
172 heated, and the phase transition in iron was bracketed between volumes and temperatures  
173 (Supplemental Table S1) that agree with the published phase diagram of Komabayashi and Fei  
174 (2010) upon heating.

175         Molar volumes of the Fe-16Si samples were determined from their measured *d*-spacings,  
176 and phase transitions were identified from the appearance and disappearance of peaks in the  
177 diffraction pattern. Melting was determined by the appearance of diffuse scattering in the pattern,  
178 sometimes accompanied by the disappearance of the peaks of one of the sample phases.

179         In the room temperature experiments, we used the unit cell volume of KBr at 300 K to  
180 calculate the pressure (Campbell et al., in prep). Again, we assume mechanical equilibrium  
181 between the Fe-Si alloy and the KBr, based on the hydrostaticity of the neon pressure medium  
182 (Klotz et al., 2009). Deviatoric stresses on the sample are small but not negligible in neon for a  
183 material as compressible as KBr, so we performed a small correction to the measured KBr lattice  
184 parameters (after Singh, 1993). Details of this correction may be found in the Supplemental

185 Material.

186 In parallel to experiments, we performed first-principles calculations based on the  
187 projected augmented wavefunction method (Blochl, 1994) of the density-functional theory  
188 (DFT), as implemented in the ABINIT package (Gonze et al., 2002, 2009; Torrent et al., 2008).  
189 We worked on three ideally stoichiometric phases: Fe<sub>3</sub>Si with the D0<sub>3</sub> structure, hcp iron, and  
190 FeSi with the B2 structure. We employ the Generalized Gradient Approximation (GGA) of DFT,  
191 in the Perdew-Burke-Erzerhof formulation (Perdew et al., 1996). We performed calculations on  
192 the D0<sub>3</sub> structure of Fe<sub>3</sub>Si with a ferromagnetic configuration, and did non-spin-polarized  
193 calculations for the other two phases, as they are non-magnetic. For Fe<sub>3</sub>Si we repeated the  
194 calculations using the Local Density Approximation (LDA). We used 15 Hartrees for the kinetic  
195 energy cutoff and 8x8x8 grids of special k points (Monkhorst and Pack, 1976) for all three  
196 phases. These parameters ensure a precision better than 1 mHa/formula unit in energy and better  
197 than 1 GPa in pressure.

198

199

### 200 **3. Results**

201

202 At pressures below ~50-65 GPa, our Fe-alloy containing 16 wt% Si was stable in the D0<sub>3</sub>  
203 (BiF<sub>3</sub>- or AlFe<sub>3</sub>-type) structure, while above these pressures it was stable as a mixture of B2  
204 (CsCl-type) and hcp phases (Figure 1). The D0<sub>3</sub> structure, which belongs to space group *Fm3m*,  
205 has been recognized in iron-silicon alloys with slightly lower silicon contents at 1 bar  
206 (Christensen et al., 2008; Massalski, 1986; Rhee, 2004), but has not previously been reported in  
207 Fe-Si alloys at high pressures and temperatures. The D0<sub>3</sub> structure can be thought of as a

208 doubling of the B2 unit cell in each dimension, with a higher degree of ordering. It produces all  
209 of the B2 diffraction peaks (the  $D0_3$  peaks with even Miller indices, which are doubled relative  
210 to the B2 Miller indices) plus several additional peaks (those  $D0_3$  peaks with odd Miller indices).  
211 Supplemental Figure S1 illustrates the  $D0_3$  structure.

212 Figure 2a and b illustrates an example of an X-ray diffraction pattern of our sample  
213 collected at 44 GPa and 1840 K, with peaks corresponding to B2-KBr and  $D0_3$  Fe-Si alloy. KBr  
214 tends to produce smooth diffraction rings, while the thinner, hotter alloy produces discrete spots  
215 (Figure 2a). Figure 2c shows a pattern collected at 137 GPa and 2130 K, with peaks from B2-  
216 KBr, B2 Fe-Si alloy, and hcp Fe-Si alloy. The KBr peaks at these high temperatures are broader  
217 than those of the sample, due to the wider range of temperatures experienced by the thicker layer  
218 of the KBr pressure medium. The lower intensity odd peaks of the  $D0_3$  structure sometimes  
219 appeared in the integrated diffraction pattern, as can be seen in Figure 2b, but frequently required  
220 examination of the 2D image to locate diffraction spots. In all of our diffraction patterns, all  
221 peaks were identified as corresponding to KBr, some structure of Fe-Si alloy, or neon (300 K  
222 data only).

223 The pressure-volume-temperature ( $P$ - $V$ - $T$ ) data from the synchrotron X-ray diffraction  
224 experiments are listed in Supplemental Table S2. The lattice parameter of  $D0_3$  Fe-Si alloy was  
225 calculated from two to ten of the following  $hkl$  peaks: 111, 200, 220, 311, 222, 400, 331, 420,  
226 511+333, 440, and 422. The lattice parameter of B2 Fe-Si alloy was calculated from two to six of  
227 the following peaks: 100, 110, 111, 200, 210, 211, 220, and 221+300. Those of hcp Fe-Si alloy,  
228 and its  $c/a$  ratio, were calculated from up to five of the following peaks: 100, 002, 101, 102, and  
229 110. KBr was stable in the B2 structure over the pressure range of interest. Its lattice parameter  
230 was determined from the observed  $d$ -spacings of four to thirteen of the following  $hkl$  peaks: 100,

231 110, 111, 200, 210, 211, 220, 221+300, 310, 311, 222, 320, and 321. Uncertainties on the lattice  
232 parameters are standard errors from the variations in lattice parameters from these  $d$ -spacings.

233 Figure 3 shows our  $P$ - $V$ - $T$  data for the  $D0_3$  structure and for the B2+hcp mixture of Fe-16Si.

234 It is not straightforward to determine the bulk molar volume of the B2+hcp mixture,  
235 because we cannot quantify the amount of each phase present. When both phases are visible in  
236 the diffraction pattern, we use the mean of the volumes of the two endmembers, with these  
237 averages plotted in Figure 3. The bulk volume of the two-phase assemblage must lie between  
238 that of the end members, so we incorporate the difference in their volumes into the uncertainty in  
239 mixture volume. This approach constrains the volume of the assemblage with acceptable  
240 uncertainty because of the similarity of the B2 and hcp volumes, which typically differ by  
241  $<0.5\%$ .

242 Also shown in Figure 3 are calculated volumes of  $Fe_3Si$  in the  $D0_3$  structure at 0 K,  
243 determined using LDA and GGA. These results are listed in Supplemental Table S3.  
244 Supplemental Table S3 also lists data on the magnetization of  $Fe_3Si$  as a function of pressure,  
245 which is illustrated in Supplemental Figure S2.

246 Figure 4 shows an example of the appearance of diffuse scattering in X-ray diffraction  
247 patterns during laser heating at 110 GPa. These diffraction patterns were all obtained with a fixed  
248 exposure time, and were offset (by  $<1\%$ ) to match intensities at  $2\theta = 5.0^\circ$ . At temperatures of  
249 3605 K and greater, a broad elevated bump in the background appears at approximately  $2\theta = 9$ -  
250  $12^\circ$ , representing the X-ray scattering by the liquid alloy. The diffuse scattering continues to  
251 increase with increasing temperature, indicating a higher fraction of partial melt. Pressures and  
252 temperatures of upper and lower bounds on melting from X-ray diffuse scattering are listed in  
253 Supplemental Table S4.

254

255

## 256 **4. Discussion**

257

### 258 ***4.1. Subsolidus phase relations***

259

260           The phase diagram of Fe-16Si had not previously been determined at the pressures and  
261 temperatures of the deep Earth. We determined this phase diagram to 140 GPa, as shown in  
262 Figure 1. We find the D0<sub>3</sub> structure stable at lower pressures and high temperatures, where  
263 studies on similar alloys observed the bcc or B2 structures (Asanuma et al., 2010; Lin et al.,  
264 2003; Zhang and Guyot, 1999). It is possible that that the D0<sub>3</sub> phase was present but not detected  
265 in these earlier studies, because it is a more ordered version of these other structures, and the X-  
266 ray diffraction peaks that indicate this higher degree of ordering are typically small and difficult  
267 to detect. In our data, they are present only as spots, not as diffraction rings (Figure 2a), and in  
268 many instances we were only able to identify these spots in the 2D diffraction image, not in the  
269 integrated patterns. At higher pressures, we find a B2+hcp mixture. This was likely undetected  
270 during compression at room temperature by Lin et al. (2003) and Hirao et al. (2004) due to a  
271 kinetic barrier of this transition; we also fail to observe the transition to a B2+hcp mixture at  
272 room temperature.

273           We find that the intensity of the hcp peaks relative to that of the B2 peaks generally  
274 increases with pressure, suggesting that the mixture contains more hcp alloy at higher pressures.  
275 This implies that at even higher pressures, beyond those of the present study, the alloy will  
276 convert completely to an hcp structure, analogous to the phase diagram of Fe-7.9Si reported by

277 Lin et al. (2002, 2009).

278           In one region of  $P$ - $T$  space, between  $\sim 50$ - $90$  GPa and  $\sim 2100$ - $2800$  K, we observe the B2  
279 structure only (Figure 1). This transition from the  $D0_3$  phase to the B2 structure represents  
280 disordering upon heating. It may be a gradual or sudden transition; this is difficult to determine  
281 due to the many diffraction peaks that are produced by both structures and the relatively low  
282 intensities of the  $D0_3$ -only (odd) peaks. Asanuma et al. (2010) reported seeing the bcc structure  
283 in this region of  $P$ - $T$  space, at  $\sim 57$  GPa and temperatures near the melting curve. This may  
284 represent a misidentification of the B2 structure, since the B2 and bcc structures share half of  
285 their diffraction peaks and the B2-only peaks are relatively low intensity compared to those of  
286 the bcc structure. Alternatively, this discrepancy may be due to differences in composition  
287 (Asanuma et al. (2010) studied Fe-18Si). Our  $P$ - $V$ - $T$  data on the B2 structure in this region were  
288 not used in any of our equation of state fits.

289           The appearance and disappearance of the hcp phase at high pressures and temperatures is  
290 abrupt, and we have used our data to constrain the slope of this phase boundary (Figure 1). We  
291 find a positive Clapeyron slope of this transition of approximately 46 K/GPa, with the phase  
292 boundary intersecting the melting curve at  $\sim 99$  GPa and  $\sim 3375$  K. Our results on the phase  
293 diagram of this alloy demonstrate that it is stable as a B2+hcp mixture at the pressures of the  
294 core-mantle boundary (136 GPa; Figure 1).

295

#### 296 **4.2. Melting curve**

297

298           The melting curve of Fe-16Si was measured to 140 GPa using synchrotron X-ray  
299 scattering measurements (Figure 5). Each data point in Figure 5 representing a lower bound from

300 the present study was the highest temperature at which diffuse scattering was not observed, and  
301 the upper bounds are the lowest temperatures at which it was observed. Our data agree well with  
302 the data of Asanuma et al. (2010) and Morard et al. (2011) up to ~60 GPa. At higher pressures,  
303 our data are broadly compatible with, though slightly higher than, those earlier studies.

304 Asanuma et al. (2010) studied the melting of Fe-18Si up to 120 GPa. They placed lower  
305 bounds on the melting point by identifying discontinuities in the laser power-temperature  
306 relationship, and placed upper bounds based on the presence of quenched texture in recovered  
307 samples. Above ~60 GPa, their melting data systematically fall a couple hundred degrees lower  
308 than ours (Figure 5). Morard et al. (2011) studied Fe-5Ni-15Si to 80 GPa using diffuse  
309 scattering. The presence of nickel in their alloy might explain divergence of our melting curves.  
310 The variation in silicon content between these three studies should not be relevant at higher  
311 pressures, where two phase eutectic melting is likely.

312 At lower pressures, below ~95 GPa (Figure 1), single phase melting occurs, from either  
313 the B2 or D0<sub>3</sub> crystal structure. Presumably Fe-16Si passes through a small solid+melt loop  
314 during melting at these pressures, but the width of this loop is not easily quantifiable using our  
315 experimental methods. Above ~95 GPa, two phase melting occurs from the mixture of the B2  
316 and hcp structures, implying the presence of a eutectic. At 137 GPa, we bracket the melting point  
317 between 3520 and 3720 K. Since there is a eutectic for this composition and pressure, 3520 K is  
318 the minimum temperature for the Earth's outer core if it were to consist exclusively of Fe-Si  
319 alloy.

320 We observed that at pressures above ~95 GPa, when our alloy was stable as a B2+hcp  
321 mixture, it was the hcp phase that disappears at the eutectic temperature, while the B2 phase  
322 remains and coexists with the melt (Figure 4). This implies that the eutectic composition in the

323 Fe-Si system over this  $P$ - $T$  region has a lower silicon content than our starting composition of 16  
324 wt%. At 21 GPa, Kuwayama and Hirose (2004) found a eutectic composition in the Fe-FeSi  
325 system of 26 wt% Si, suggesting that the eutectic is shifting to more iron-rich compositions with  
326 increasing pressure. Alternatively, the eutectic we report here might be a different one than that  
327 identified by Kuwayama and Hirose (2004). Further work is necessary to better resolve the  
328 evolution of the eutectic in the Fe-Si system at high pressures.

329         The melting curve is thermodynamically required to have a kink in it where it intersects  
330 the subsolidus phase boundary, but this is not resolvable in our melting data. In Figures 1 and 5,  
331 we illustrate an approximate melting curve that includes a small kink at 95 GPa, where our  
332 bounds on melting reach the extrapolated boundary between the  $D0_3$  and B2+hcp phase fields.

333         Even very thin samples will sustain an axial temperature gradient of a few percent  
334 (Campbell et al., 2007, 2009). When determining melting, we use the measured sample  
335 temperatures without correcting for an axial temperature gradient. The measured temperature  
336 should reflect the temperature at the surface of the sample, where it is the hottest, which is where  
337 melting begins. However, since it is uncertain how much partial melt must be present in the  
338 volume probed by the X-ray for liquid scattering to be efficient enough to be detected, our  
339 measurements may slightly overestimate the true melting point.

340

### 341 ***4.3. Equations of state***

342

343         We fit our  $P$ - $V$ - $T$  dataset for  $D0_3$  Fe-16Si to a Mie-Grüneisen equation of state,

$$344 \quad P(V,T) = P_{300}(V) + (\gamma/V)[E(\theta_D,T) - E_{300}(\theta_D,300)] \quad (1)$$

345 with the 300 K isothermal pressure ( $P_{300}$ ) described by the third-order Birch-Murnaghan

346 equation of state (Birch, 1952), and the thermal pressure term based on a Debye model of  
347 vibrational energy ( $E$ ), with Grüneisen parameter  $\gamma = \gamma_0(V/V_0)^q$  and Debye temperature  $\theta_D =$   
348  $\theta_0 \exp[\gamma_0 (1 - (V/V_0)^q)/q]$ . We did not explicitly include any anharmonic or electronic  
349 contributions to the thermal pressure, instead allowing all thermal pressure variation to be  
350 described by  $\gamma$  and  $q$  (e.g. Fei et al., 2007). This reduced the number of fitted parameters, which  
351 was necessary given the resolution of our data.

352 Table 2 shows the equation of state parameters we found for D0<sub>3</sub> Fe-16Si alloy. We fit  
353 the one bar isothermal bulk modulus ( $K_0$ ) and its pressure derivative ( $K_0'$ ) using only the room  
354 temperature compression data, fixing the zero-pressure volume to the value we measured  
355 experimentally. We then fit the one bar Grüneisen parameter ( $\gamma_0$ ) from the high temperature data,  
356 fixing the one bar Debye temperature ( $\theta_0$ ) to that of hcp-iron (417 K, from Dewaele et al., 2006)  
357 and fixing  $q$  to one. Our value for  $K_0$  for D0<sub>3</sub> Fe-16Si alloy is similar to that reported in the static  
358 compression study of Lin et al. (2003) for Fe-17Si ( $193.4 \pm 4.8$  GPa vs.  $199.0 \pm 5.3$  GPa), but we  
359 found a slightly lower value of  $K_0'$  than Lin et al. (2003) ( $4.91 \pm 0.59$  vs.  $5.66 \pm 0.61$ ). Our zero  
360 pressure volume,  $6.799 \pm 0.004$  cm<sup>3</sup>/mol, is also smaller than that found by Lin et al. (2003)  
361 ( $6.887 \pm 0.007$  cm<sup>3</sup>/mol), but larger than the values predicted by Christensen et al. (2008) ( $6.631$   
362 cm<sup>3</sup>/mol) and Rhee (2004) ( $6.642$  cm<sup>3</sup>/mol), and slightly larger than that measured by Mishra et  
363 al. (1985) ( $6.789 \pm 0.09$  cm<sup>3</sup>/mol).

364 As expected, theoretical volumes calculated using LDA (Figure 3) are lower than those  
365 predicted from our equation of state at 0 K by ~9%, but they show similar compressibility to the  
366 experimental data. GGA yields a higher one bar volume than we measured experimentally ( $6.907$   
367 cm<sup>3</sup>/mol), but also predicts a higher compressibility. With this tradeoff, there is excellent  
368 agreement (<1% volume difference) between the experimentally determined volumes and those

369 calculated using GGA at 20 and 40 GPa. The EOS fit to the static (0 K) GGA results yield  $V_0 =$   
370  $6.851 \text{ cm}^3/\text{mol}$ ,  $K_0 = 200 \text{ GPa}$ , and  $K_0' = 4.44$ . Similar relationships between data obtained  
371 experimentally versus by LDA and GGA have already been recorded in previous studies on the  
372 Fe-Si system (Vočadlo et al., 1999; Moroni et al., 1999; Caracas and Wentzcovitch, 2005). The  
373 magnetization of  $\text{Fe}_3\text{Si}$  decreases smoothly with decreasing volume and increasing pressure  
374 (Supplemental Figure S2), and remains positive even at core pressures.

375 We have also determined an equation of state for the B2+hcp mixture of our alloy by  
376 fitting our data to a Mie-Grüneisen equation of state as described above. The resulting equation  
377 of state parameters are listed in Table 2. It is not typical to construct an equation of state for a  
378 two-phase mixture, but in this case there was no better alternative, since we have no knowledge  
379 of how silicon partitioning between the two phases varies with pressure and temperature or of the  
380 relative abundances of the two phases. In addition, constructing an equation of state for the  
381 mixture seems justified in this case, because the volume difference between the B2 and hcp  
382 phases is small (mean of  $0.4\% \pm 0.6\%$ ). The modal abundances of B2 and hcp are varying with  
383 pressure and partitioning silicon in such a way as to keep the bulk composition fixed. Finally,  
384 this approximation is validated by the fact that the goal is to make a comparison to the Earth's  
385 core at core-mantle boundary conditions (Section 4.4), not to establish the mixture's physical  
386 parameters.

387 For the B2+hcp mixture, we fit  $K_0$  and  $\gamma_0$  (Table 2). We fixed  $V_0$  to that of the  $\text{D0}_3$   
388 structure,  $\theta_0$  to that of hcp-iron (Dewaele et al., 2006), and  $q = 1$ . We also fixed  $K_0'$ , finding the  
389 best fit to our data with  $K_0' = 4$ . We find a lower value of  $K_0'$  and a higher value of  $K_0$  for the  
390 B2+hcp mixture than for the  $\text{D0}_3$  structure. We find very similar values of  $\gamma_0$  for the  $\text{D0}_3$  phase  
391 and the B2+hcp mixture. Isotherms calculated from our equations of state are shown in Figure 3

392 for a variety of temperatures.

393         The hcp Fe-Si phase has a slightly larger volume than the B2 Fe-Si phase under almost  
394 all experimental conditions investigated. This may be due to silicon partitioning between the two  
395 phases producing a more iron-rich hcp phase. Since we expect the hcp structure to be the high  
396 pressure phase (Section 4.1), it should have a greater molar density than the B2 phase for a fixed  
397 composition, but the slightly larger volume can be explained by its higher Fe content. We find no  
398 obvious pressure or temperature dependence on the volume difference between the two phases.  
399 This further justifies our use of a single equation of state to describe the two-phase mixture.

400         These considerations are supported by the first-principles results. The static equation of  
401 state of hcp-Fe has  $V_0 = 6.466 \text{ cm}^3/\text{mol}$ ,  $K_0 = 244 \text{ GPa}$ , and  $K_0' = 4.55$ , while B2-FeSi has a  
402 static equation of state with  $V_0 = 6.523 \text{ cm}^3/\text{mol}$ ,  $K_0 = 220 \text{ GPa}$ , and  $K_0' = 4.39$ . Calculated  $P$ - $V$   
403 data for these phases are shown in Supplemental Tables 5 and 6, respectively. Regardless of the  
404 relative volumes at one bar, differences in compressibility within the stability field of the hcp and  
405 B2 phases produce the same relative relation as seen experimentally: hcp-Fe has a larger volume  
406 than B2-FeSi. The volume difference is slightly enhanced by increasing pressure, but it remains  
407 less than 1.8% even at 200 GPa. The corresponding stoichiometric mechanical mixture, an  
408 average of the B2 and hcp phases, yields an EOS with  $V_0 = 6.4925 \text{ cm}^3/\text{mol}$ ,  $K_0 = 234 \text{ GPa}$ , and  
409  $K_0' = 4.43$ .

410         Supplemental Table S2 lists the  $c/a$  ratio for the hcp Fe-Si phase. It is fairly constant over  
411 the entire  $P$ - $T$  range explored, though it decreases slightly with pressure, from  $\sim 1.620$  near 70  
412 GPa to  $\sim 1.615$  at 135 GPa. It does not have any resolvable temperature dependence.

413

414 **4.4. Comparison to the core density deficit**

415

416 Earth's core is known to be an iron rich alloy, yet the density of the core is lower than that  
417 of pure iron under the appropriate pressure-temperature conditions; this difference is known as  
418 the core density deficit. Assuming that the Earth's core may be predominantly an Fe-Si alloy, we  
419 can place constraints on the silicon content of the core by comparing the equation of state of Fe-  
420 Si alloys to the seismologically determined density profile in the outer core. Since our alloy is  
421 stable as a B2+hcp mixture at core-mantle boundary pressures, it is the equation of state of this  
422 mixture that we apply to calculations of the core density deficit. We use a core-mantle boundary  
423 (CMB) pressure of 135.8 GPa and a density of  $9.9 \text{ g/cm}^3$  in the outer core at the CMB from  
424 PREM (Dziewonski and Anderson, 1981). The outer core temperature at the CMB is taken to be  
425  $4000 \pm 500 \text{ K}$ , based on the analysis of Anderson (2003). We assume that the outer core  
426 temperature profile is adiabatic (Birch, 1952), and that iron and iron-rich alloys experience a 1-  
427 2% volume increase upon melting at core pressures (Anderson, 2003). Although it is likely that  
428 the outer core contains more than one light element, such as Si, S, O, and/or C (McDonough,  
429 2003), for this analysis we consider an outer core whose light element component is comprised  
430 solely of silicon.

431 Figure 6 illustrates the density difference between pure solid hcp-iron, calculated along  
432 an adiabat from the equation of state of Dewaele et al. (2006), and PREM, the seismologically  
433 determined density of the Earth's outer core (Dziewonski and Anderson, 1981). Based on the  
434 assumptions outlined above, we find that PREM at the CMB is  $10.4 \pm 0.9\%$  less dense than solid  
435 hcp-Fe at the same conditions. Approximately 1-2% of this density deficit can be explained by  
436 the volume change that iron experiences upon melting at high pressures (Anderson, 2003), but  
437 the remainder of this deficit must be due to the presence of light elements in the outer core, such

438 as silicon.

439 Our equation of state for the B2+hcp mixture of Fe-16Si can be used to constrain the  
440 amount of silicon required to match the density deficit in the Earth's outer core. This analysis  
441 requires no extrapolation in pressure and only a small extrapolation in temperature to apply our  
442 equation of state at CMB conditions. We corrected the outer core density to account for a Ni/Fe  
443 atomic ratio of 0.058 in the core (McDonough, 2003). A silicon content of  $11.3 \pm 1.5$  wt% is  
444 required to match PREM in the outer core at the CMB for a purely Fe-Ni-Si outer core. The  
445 uncertainty in this calculation is based upon the stated uncertainties in the CMB temperature, the  
446 volume change of melting, and the equation of state, with the uncertainty in CMB temperature  
447 dominating. Varying the amount of nickel in the core has very little effect on the amount of  
448 silicon needed to match PREM (less than  $\pm 0.1$  wt%).

449 The core's light element component is likely to be comprised of multiple light elements,  
450 which may or may not include silicon. If the core contains other light elements, then 11.3 wt% is  
451 effectively the maximum amount of silicon that may exist in the Earth's outer core, with the  
452 remainder of the core density deficit being comprised of other light elements. This composition  
453 is consistent with a eutectic in the Fe-Si system of less than 16 wt% Si, as established above,  
454 because the coexisting solid phase (inner core) must be more Fe-rich. Assuming that this eutectic  
455 composition doesn't decrease dramatically at higher pressures, it is plausible on this basis that  
456 silicon could be the dominant light element in the Earth's core.

457 Figure 6 shows that the density profile of the B2+hcp mixture of our alloy approximately  
458 matches the slope of PREM when its equation of state is extrapolated through the  $P$ - $T$  range of  
459 the Earth's outer core. This is not the case for density profiles of FeO (Fischer et al., 2011) and  
460 Fe<sub>3</sub>S (Seagle et al., 2006) calculated from their published equations of state. This lends support

461 to the idea that silicon is the dominant light element in the Earth's core. However, this  
462 comparison to PREM does require large extrapolations in the equations of state of these alloys,  
463 and alternative explanations for variations in density profile slopes have been proposed (Fischer  
464 et al., 2011).

465         A similar calculation may be performed to assess the amount of silicon needed to match  
466 the density deficit of the Earth's inner core. We assume an inner core boundary (ICB)  
467 temperature of  $5000 \pm 1000$  K (Boehler, 2000), pressure of 328.85 GPa, and density of the inner  
468 core of  $12.76 \text{ g/cm}^3$  at the ICB (Dziewonski and Anderson, 1981). The density was again  
469 corrected for a Ni/Fe atomic ratio of 0.058 in the core (McDonough, 2003). Under these  
470 assumptions, for an Fe-Si-Ni inner core, the density deficit at the ICB can be explained by the  
471 presence of  $7.7 \pm 1.3$  wt% silicon in the inner core. However, it should be emphasized that this  
472 calculation requires large extrapolations in temperature, pressure, and silicon content. This  
473 calculation is also performed with the equation of state of the B2+hcp mixture. While we predict  
474 an eventual transition to the hcp structure at higher pressures, this transition is unlikely to have a  
475 very large effect on the density of our alloy, since the relative proportions of B2 and hcp  
476 structures are changing gradually across the phase loop. Nevertheless, this extrapolation should  
477 be used with caution.

478

479

## 480 **5. Conclusions**

481

482         The phase diagram of an iron-silicon alloy containing 16 wt% silicon has been  
483 determined to high temperatures and pressures reaching those of the Earth's outer core. This

484 phase diagram includes the  $D0_3$  structure, which has not previously been reported in an Fe-Si  
485 alloy at high pressures and temperatures, and the location and slope of the phase boundary  
486 between the  $D0_3$  structure and a B2+hcp mixture at higher pressures and temperatures has been  
487 measured. Equations of state of this alloy's  $D0_3$  structure and its B2+hcp assemblage were also  
488 determined. The eutectic composition in the Fe-Si system at CMB conditions is less than 16 wt%  
489 silicon. The melting curve indicates that 3520 K is a minimum temperature for the Earth's outer  
490 core, if it consists exclusively of Fe-Si alloy. LDA calculations accurately predict the  
491 compressibility of  $D0_3$   $Fe_3Si$ , whereas GGA calculations match its volume at high pressures.

492         The equation of state for the B2+hcp mixture of Fe-16Si can be compared to that of hcp-  
493 Fe (Dewaele et al., 2006) and PREM, the seismologically determined density of the Earth's outer  
494 core (Dziewonski and Anderson, 1981) to perform an analysis of the core density deficit. For an  
495 outer core containing only iron, nickel, and silicon,  $11.3 \pm 1.5$  wt% silicon would be required to  
496 match PREM at the core-mantle boundary, making this the maximum amount of silicon that may  
497 exist in the Earth's outer core.

498

499

## 500 **References**

501

502 Allègre, C.J., Poirier, J.-P., Humler, E., Hofmann, A.W., 1995. The chemical composition of the  
503 Earth. *Earth Planet. Sci. Lett.* 134, 515-526.

504 Anderson, O.L., 2003. The three-dimensional phase diagram of iron. In: Dehant, V., Creager,

505 K.C., Karato, S.-I., Zatman, S. (Eds.), *Earth's Core: Dynamics, Structure, Rotation.*

506 American Geophysical Union, Washington, DC.

507 Asanuma, H., Ohtani, E., Sakai, T., Terasaki, H., Kamada, S., Kondo, T., Kikegawa, T., 2010.  
508 Melting of iron-silicon alloy up to the core-mantle boundary pressure: Implications to the  
509 thermal structure of the Earth's core. *Phys. Chem. Minerals* 37, 353-359.

510 Balchan, A.S., Cowen, G.R., 1966. Shock compression of two iron-silicon alloys to 2.7  
511 megabars. *J. Geophys. Res.* 71, 3577-3588.

512 Birch, F., 1952. Elasticity and constitution of the Earth's interior. *J. Geophys. Res.* 37, 227-286.

513 Blochl, P.E., 1994. Projector augmented-wave method. *Phys. Rev. B* 50, 17953–17979.

514 Boehler, R., 2000. High-pressure experiments and the phase diagram of lower mantle and core  
515 materials. *Rev. Geophys.* 38, 221-245.

516 Campbell, A.J., Fischer, R.A., Prakapenka, V.B., in preparation. Equation of state of potassium  
517 bromide: Applications to pressure calibration in laser-heated diamond anvil cell experiments.

518 Campbell, A.J., Seagle, C.T., Heinz, D.L., Shen, G., Prakapenka, V.B., 2007. Partial melting in  
519 the iron-sulfur system at high pressure: A synchrotron X-ray diffraction study. *Phys. Earth  
520 Planet. Inter.* 162, 119-128.

521 Campbell, A.J., Danielson, L., Richter, K., Seagle, C.T., Wang, Y., Prakapenka, V.B., 2009.  
522 High pressure effects on the iron-iron oxide and nickel-nickel oxide oxygen fugacity buffers.  
523 *Earth Planet. Sci. Lett.* 286, 556-564.

524 Caracas, R., Wentzcovitch, R., 2004. Equation of state and elasticity of FeSi. *Geophys. Res. Lett.*  
525 31, L20603.

526 Christensen, N.E., Kudrnovsky, J., Rodriguez, C.O., 2008. Metamagnetic behavior in Fe<sub>3</sub>Si and  
527 Fe<sub>3</sub>Al. *Int. J. Nanoelectrics and Materials* 1, 1-15.

528 Côté, A.S., Vočadlo, L., Brodholt, J.P., 2008. The effect of silicon impurities on the phase  
529 diagram of iron and possible implications for the Earth's core structure. *J. Phys. Chem.*

530 Solids 69, 2177-2181.

531 Dewaele, A., Loubeyre, P., Occelli, F., Mezouar, M., Dorogokupets, P.I., Torrent, M., 2006.

532 Quasihydrostatic equation of state of iron above 2 Mbar. Phys. Rev. Lett. 97, 215504.

533 Dewaele, A., Datchi, F., Loubeyre, P., Mezouar, M., 2008. High pressure-high temperature

534 equations of state of neon and diamond. Phys. Rev. B 77, 094106.

535 Dziewonski, A.M., Anderson, D.L., 1981. Preliminary reference Earth model. Phys. Earth

536 Planet. Inter. 25, 297-356.

537 Fei, Y., Ricolleau, A., Frank, M., Mibe, K., Shen, G., Prakapenka, V., 2007. Toward an

538 internally consistent pressure scale. Proc. Natl. Acad. Sci. U.S.A. 104, 9182-9186.

539 Fischer, R.A., Campbell, A.J., Shofner, G.A., Lord, O.T., Dera, P., Prakapenka, V.B., 2011.

540 Equation of state and phase diagram of FeO. Earth Planet. Sci. Lett. 304, 496-502.

541 Fitoussi, C., Bourdon, B., Kleine, T., Oberli, F., Reynolds, B.C., 2009. Si isotope systematic of

542 meteorites and terrestrial peridotites: Implications for Mg/Si fractionation in the solar nebula

543 and for Si in the Earth's core. Earth Planet. Sci. Lett. 287, 77-85.

544 Georg, R.B., Halliday, A.N., Schauble, E.A., Reynolds, B.C., 2007. Silicon in the Earth's core.

545 Nature 447, 1102-1106.

546 Gonze, X., Beuken, J.-M., Caracas, R., Detraux, F., et al., 2002. First-principles computation of

547 material properties: the ABINIT software project. Comput. Mater. Sci. 25, 478-492.

548 Gonze, X., Amadon, B., Anglade, P.-M., Beuken, J.-M., et al., 2009. ABINIT: First-principles

549 approach to material and nanosystem properties. Comp. Phys. Comm. 180, 2582-2816.

550 Hammersley, A.P., Svensson, S.O., Hanfland, M., Fitch, A.N., Hausermann, D., 1996. Two-

551 dimensional detector software: From real detector to idealized image or two-theta scan. High

552 Press. Res. 14, 235-248.

553 Heinz, D.L., Jeanloz, R., 1987. Temperature measurements in the laser-heated diamond cell, in:  
554 Manghnani, M.H., Syono, Y. (Eds.), High-Pressure Research in Mineral Physics. Terra  
555 Scientific Publishing, Tokyo / American Geophysical Union, Washington, DC.

556 Hirao, N., Ohtani, E., Kondo, T., Kikegawa, T., 2004. Equation of state of iron-silicon alloys to  
557 megabar pressure. *Phys. Chem. Minerals* 31, 329-336.

558 Hu, J.Z., Mao, H.K., Shu, J.F., Guo, Q.Z., Liu, H.Z., 2006. Diamond anvil cell radial x-ray  
559 diffraction program at the National Synchrotron Light Source. *J. Phys.: Condens. Matter* 18,  
560 S1091-S1096.

561 Javoy, M., Kaminski, E., Guyot, F., Andrault, D., Sanloup, C., Moreira, M., Labrosse, S.,  
562 Jambon, A., Agrinier, P., Davaille, A., Jaupart, C., 2010. The chemical composition of the  
563 Earth: Enstatite chondrite models. *Earth Planet. Sci. Lett.* 293, 259-268.

564 Keil, K., Berkley, J.L., Fuchs, L.H., 1982. Suessite, Fe<sub>3</sub>Si: A new mineral in the North Haig  
565 ureilite. *Am. Mineral.* 67, 126-131.

566 Klotz, S., Chervin, J.-C., Munsch, P., Le Marchand, G., 2009. Hydrostatic limits of 11 pressure  
567 transmitting media. *J. Phys. D: Appl. Phys.* 42, 075413.

568 Knittle, E., Jeanloz, R., 1991. Earth's core-mantle boundary: Results of experiments at high  
569 pressures and temperatures. *Science* 251, 1438-1443.

570 Komabayashi, T., Fei, Y., 2010. Internally consistent thermodynamic database for iron to the  
571 Earth's core conditions. *J. Geophys. Res.* 115, B03202.

572 Kunz, M., MacDowell, A.A., Caldwell, W.A., Cambie, D., Celestre, R.S., Domning, E.E.,  
573 Duarte, R.M., Gleason, A.E., Glossinger, J.M., Kelez, N., Plate, D.W., Yu, T., Zaug, J.M.,  
574 Padmore, H.W., Jeanloz, R., Alivisatos, A.P., Clark, S.M., 2005. A beamline for high-  
575 pressure studies at the Advanced Light Source with a superconducting bending magnet as the

576 source. *J. Synchrotron Rad.* 12, 650-658.

577 Kuwayama, Y., Hirose, K., 2004. Phase relations in the system Fe-FeSi at 21 GPa. *Am. Mineral.*  
578 89, 273-276.

579 Lin, J.-F., Heinz, D.L., Campbell, A.J., Devine, J.M., Shen, G., 2002. Iron-silicon alloy in  
580 Earth's core? *Science* 295, 313-315.

581 Lin, J.-F., Campbell, A.J., Heinz, D.L., Shen, G., 2003. Static compression of iron-silicon alloys:  
582 Implications for silicon in the Earth's core. *J. Geophys. Res.* 108, 2045.

583 Lin, J.-F., Scott, H.P., Fischer, R.A., Chang, Y.-Y., Kantor, I., Prakapenka, V.B., 2009. Phase  
584 relations of Fe-Si alloy in Earth's core. *Geophys. Res. Lett.* 36, L06306.

585 Malavergne, V., Siebert, J., Guyot, F., Gautron, L., Combes, R., Hammouda, T., Borensztajn, S.,  
586 Frost, D., Martinez, I., 2004. Si in the core? New high-pressure and high-temperature  
587 experimental data. *Geochim. Cosmochim. Acta* 68, 4201-4211.

588 Mao, H.K., Xu, J., Bell, P.M., 1986. Calibration of the ruby pressure gauge to 800 kbar under  
589 quasi-hydrostatic conditions. *J. Geophys. Res.* 91, 4673-4676.

590 Massalski, T.B., 1986. *Binary Alloy Phase Diagrams*. American Society for Metals, Metals Park,  
591 Ohio.

592 McDonough, W.F., 2003. Compositional model for the Earth's core. In: Carlson, R.W. (Ed.),  
593 *Treatise of Geochemistry*, Vol. 2. Elsevier-Pergamon, Oxford, pp. 547-568.

594 Miller, N.A., 2009. Melting and phase relations in iron-silicon alloys with applications to the  
595 Earth's core. M.S. thesis, University of Maryland.

596 Mishra, S.N., Rambabu, D., Grover, A.K., Pillay, R.G., Tandon, P.N., Devare, H.G.,  
597 Vijayaraghavan, R., 1985. Mössbauer and magnetization studies in Fe<sub>3-x</sub>Ru<sub>x</sub>Si. *J. Appl. Phys.*  
598 57, 3258-3260.

599 Monkhorst, H.J., Pack, J.D., 1976. Special points for Brillouin-zone integrations. Phys. Rev. B  
600 13, 5188–5192.

601 Morard, G., Andrault, D., Guignot, N., Siebert, J., Garbarino, G., Antonangeli, D., 2011. Melting  
602 of Fe-Ni-Si and Fe-Ni-S alloys at megabar pressures: Implications for the core-mantle  
603 boundary temperature. Phys. Chem. Minerals. 38, 767-776.

604 Moroni, E.G., Wolf, W., Hafner, J., Podloucky, R., 1999. Cohesive, structural, and electronic  
605 properties of Fe-Si compounds. Phys. Rev. B 59, 12860-12871.

606 Ozawa, H., Hirose, K., Mitome, M., Bando, Y., Sata, N., Ohishi, Y., 2009. Experimental study of  
607 reaction between perovskite and molten iron to 146 GPa and implications for chemically  
608 distinct buoyant layer at the top of the core. Phys. Chem. Minerals. 36, 355-363.

609 Perdew, J.P., Burke, K., Ernzerhof, M., 1996. Generalized gradient approximation made simple.  
610 Phys. Rev. Lett. 77, 3865-3868.

611 Prakapenka, V.B., Kuba, A., Kuznetsov, A., Laskin, A., Shkurikhin, O., Dera, P., Rivers, M.L.,  
612 Sutton, S.R., 2008. Advanced flat top laser heating system for high pressure research at  
613 GSECARS: Application to the melting behavior of germanium. High Press. Res. 28, 225-  
614 235.

615 Rhee, J.Y., 2004. Pressure dependent metamagnetism of  $Fe_3M$  ( $M = Al$  and  $Si$ ) alloys. J. Korean  
616 Phys. Soc. 45, 6-8.

617 Ricolleau, A., Fei, Y., Corgne, A., Siebert, J., Badro, J., 2011. Oxygen and silicon contents of  
618 Earth's core from high pressure metal-silicate partitioning experiments. Earth Planet. Sci.  
619 Lett. 310, 409-421.

620 Ringwood, A.E., 1959. On the chemical evolution and densities of the planets. Geochim.  
621 Cosmochim. Acta 15, 257-283.

622 Rivers, M., Prakapenka, V.B., Kubo, A., Pullins, C., Holl, C.M., Jacobsen, S.D., 2008. The  
623 COMPRES/GSECARS gas-loading system for diamond anvil cells at the Advanced Photon  
624 Source. *High Press. Res.* 28, 273-292.

625 Seagle, C.T., Campbell, A.J., Heinz, D.L., Shen, G., Prakapenka, V.B., 2006. Thermal equation  
626 of state of Fe<sub>3</sub>S and implications for sulfur in Earth's core. *J. Geophys. Res.* 111, B06209.

627 Shahar, A., Ziegler, K., Young, E.D., Ricolleau, A., Schauble, E.A., Fei, Y., 2009.  
628 Experimentally determined Si isotope fractionation between silicate and Fe metal and  
629 implications for Earth's core formation. *Earth Planet. Sci. Lett.* 288, 228-234.

630 Shen, G., Rivers, M.L., Wang, Y., Sutton, S.R., 2005. Facilities for high-pressure research with  
631 the diamond anvil cell at GSECARS. *J. Synchrotron Rad.* 12, 642-649.

632 Singh, A.K., 1993. The lattice strains in a specimen (cubic system) compressed  
633 nonhydrostatically in an opposed anvil device. *J. Appl. Phys.* 73, 4278-4286.

634 Speziale, S., Zha, C.-S., Duffy, T.S., Hemley, R.J., Mao, H.-k., 2001. Quasi-hydrostatic  
635 compression of magnesium oxide to 52 GPa: Implications for the pressure-volume-  
636 temperature equation of state. *J. Geophys. Res.* 106, 515-528.

637 Takafuji, N., Hirose, K., Mitome, M., Bando, Y., 2005. Solubilities of O and Si in liquid iron in  
638 equilibrium with (Mg,Fe)SiO<sub>3</sub> perovskite and the light elements in the core. *Geophys. Res.*  
639 *Lett.* 32, L06313.

640 Torrent, M., Jollet, F., Bottin, F., Zerah, G., Gonze, X., 2008. Implementation of the projector  
641 augmented-wave method in the ABINIT code: Application to the study of iron under  
642 pressure. *Comput. Mater. Sci.* 42, 337-351.

643 Vočadlo, L., Price, G.D., Wood, I.G., 1999. Crystal structure, compressibility and possible phase  
644 transitions in ε-FeSi studied by first-principles pseudopotential calculations. *Acta*

645 Crystallogr., Sect. B Struct. Sci., 55, 484–493.  
646 Yu, X., Secco, R.A., 2008. Equation of state of liquid Fe-17 wt%Si to 12 GPa. High Press. Res.  
647 28, 19-28.  
648 Zhang, F., Oganov, A.R., 2010. Iron silicides at pressures of the Earth's inner core. Geophys.  
649 Res. Lett. 37, L02305.  
650 Zhang, J., Guyot, F., 1999. Experimental study of the bcc-fcc phase transformations in the Fe-  
651 rich system Fe-Si at high pressures. Phys. Chem. Minerals 26, 419-424.

652

653

#### 654 **Acknowledgments**

655 We wish to acknowledge Zhiqiang Chen, Jason Knight, Alastair MacDowell, and Jinyuan Yan,  
656 beamline scientists who assisted us during this research. We would also like to thank Gwen Gage  
657 for her assistance at the beamline, Maria Valdes for help with sample preparation, and Sergey  
658 Tkachev for assistance with gas-loading. This material is based upon work supported by a  
659 National Science Foundation (NSF) Graduate Research Fellowship to R.A.F. This work was also  
660 supported by the NSF by grant EAR-0847217 to A.J.C. Portions of this work were performed at  
661 GeoSoilEnviroCARS (Sector 13), Advanced Photon Source (APS), Argonne National  
662 Laboratory. GeoSoilEnviroCARS is supported by the NSF - Earth Sciences (EAR-0622171) and  
663 Department of Energy (DOE)- Geosciences (DE-FG02-94ER14466). Use of the APS was  
664 supported by the U. S. DOE, Office of Science, Office of Basic Energy Sciences, under Contract  
665 No. DE-AC02-06CH11357. This research was partially supported by COMPRES, the  
666 Consortium for Materials Properties Research in Earth Sciences under NSF Cooperative  
667 Agreement EAR 10-43050. Use of the National Synchrotron Light Source, Brookhaven National

668 Laboratory, was supported by the U.S. DOE, Office of Science, Office of Basic Energy Sciences,  
669 under Contract No. DE-AC02-98CH10886. The Advanced Light Source is supported by the  
670 Director, Office of Science, Office of Basic Energy Sciences, of the U.S. DOE under Contract  
671 No. DE-AC02-05CH11231.

672 **Figure Captions**

673

674 **Figure 1:** High  $P$ - $T$  phase diagram of Fe-16Si alloy. Red triangles:  $D0_3$  structure. Purple  
675 diamonds: B2 structure only. Blue circles: B2+hcp mixture. Black line represents the appearance  
676 of the hcp phase at high pressures. Grey dashed curve: approximate melting curve, based on  
677 Figure 5.

678

679 **Figure 2:** A: Diffraction image before integration, collected at 44 GPa and 1840 K. White tick  
680 marks represent KBr peaks, and red tick marks represent Fe-16Si alloy peaks. B: Diffraction  
681 pattern from part A, integrated azimuthally. Peaks correspond to B2-KBr and  $D0_3$  Fe-Si alloy. C:  
682 Diffraction pattern collected at 137 GPa and 2130 K, with peaks from B2-KBr, B2 Fe-Si alloy,  
683 and hcp Fe-Si alloy. These patterns were collected using an X-ray wavelength of  $\lambda=0.3344$  Å.

684

685 **Figure 3:** Equations of state and  $P$ - $V$ - $T$  data of  $D0_3$  Fe-Si alloy, and of the mixture of B2+hcp  
686 structures of Fe-Si alloy. All data and isotherms are color-coded by temperature range according  
687 to the legend. Triangles indicate volumes of the  $D0_3$  structure, and diamonds indicate averages of  
688 the volumes of the B2 and hcp phases.  $\times$  symbols and crosses indicate volumes of  $D0_3$  Fe<sub>3</sub>Si,  
689 calculated at 0 K using LDA and GGA methods, respectively. Isotherms are calculated using the  
690 parameters in Table 2 for the midpoint of the temperature range indicated, and they do not  
691 extend above the melting curve. Solid curves are isotherms for the  $D0_3$  structure, while dashed  
692 curves are isotherms for the B2+hcp mixture.

693

694 **Figure 4:** Diffuse scattering in X-ray diffraction patterns at 110 GPa, color-coded according to

695 temperature. The bump in the background at approximately  $2\theta = 9-12^\circ$  at the highest  
696 temperatures represents scattering by the liquid alloy, bracketing the melting point between 3430  
697 K and 3605 K.

698

699 **Figure 5:** Melting data on iron-silicon alloy. Data shown are for Fe-16Si alloy (this study, red  
700 circles), Fe-5Ni-15Si (Morard et al., 2011, green triangles), and Fe-18Si (Asanuma et al., 2010,  
701 orange diamonds). Open symbols represent lower bounds, while solid symbols represent upper  
702 bounds. This study and Morard et al. (2011) determined bounds on melting using X-ray diffuse  
703 scattering. Asanuma et al. (2010) placed lower bounds using laser power-temperature  
704 discontinuities, and upper bounds based on quench texture of recovered samples. Phase  
705 identification and appearance of hcp phase (black line) are based on data shown in Figure 1.  
706 Melting curve is the same as in Figure 1.

707

708 **Figure 6:** Comparison to the core density deficit. Black curve: PREM (Dziewonski and  
709 Anderson, 1981). Blue curve: density profile for solid B2+hcp Fe-16Si, calculated from the  
710 equation of state parameters listed in Table 2. Orange curve: density profile for solid hcp-Fe,  
711 calculated from the equation of state of Dewaele et al. (2006). Solid curves follow an adiabatic  
712 temperature profile for a CMB temperature of 4000 K. Dashed curves indicate the effect of a 500  
713 K uncertainty in the CMB temperature, which is the dominant uncertainty when evaluating the  
714 core density deficit. As discussed in the text, these equations of state impose an upper bound on  
715 the silicon content of the outer core of  $11.3 \pm 1.5$  wt%.

716

717 **Table 1:** Equation of state parameters for B2-KBr used for pressure calibration, from Campbell

718 et al. (in prep). Entries with no stated uncertainties were held fixed in the fit.

719

	B2 KBr
$V_0$ (cm <sup>3</sup> /mol)	37.901
$K_0$ (GPa)	21.04 ± 0.08
$K_0'$	4.55 ± 0.01
$\theta_0$ (K)	290
$\gamma_0$	1.37 ± 0.10
$q$	1

720

721

722 **Table 2:** Equation of state parameters for D0<sub>3</sub> Fe-Si alloy, and for the B2+hcp mixture of Fe-Si

723 alloy. Zero pressure volume of the B2+hcp mixture was set equal to that of the D0<sub>3</sub> structure.

724 Zero pressure Debye temperatures ( $\theta_0$ ) were set to the value for iron (Dewaele et al., 2006).

725 Entries with no stated uncertainties (and the zero pressure volume of the D0<sub>3</sub> structure, which

726 was measured experimentally) were held fixed in the fits.

727

	D0 <sub>3</sub> Fe-Si alloy	B2+hcp Fe-Si alloy
$V_0$ (cm <sup>3</sup> /mol)	6.799 ± 0.004	6.799
$K_0$ (GPa)	193.4 ± 4.8	206.5 ± 2.0
$K_0'$	4.91 ± 0.59	4
$\theta_0$ (K)	417	417
$\gamma_0$	1.89 ± 0.06	1.80 ± 0.10
$q$	1	1

728

Figure 1

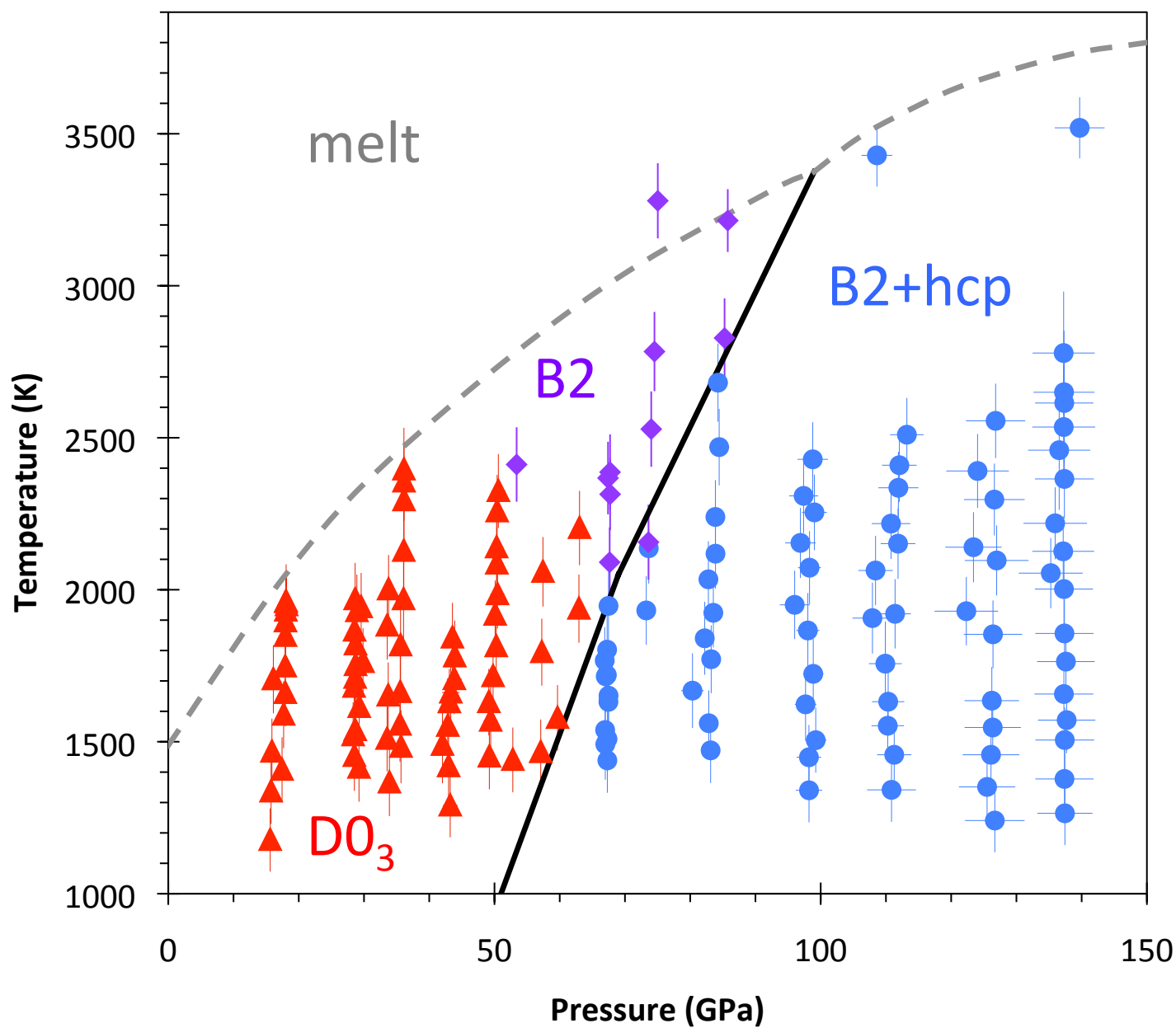
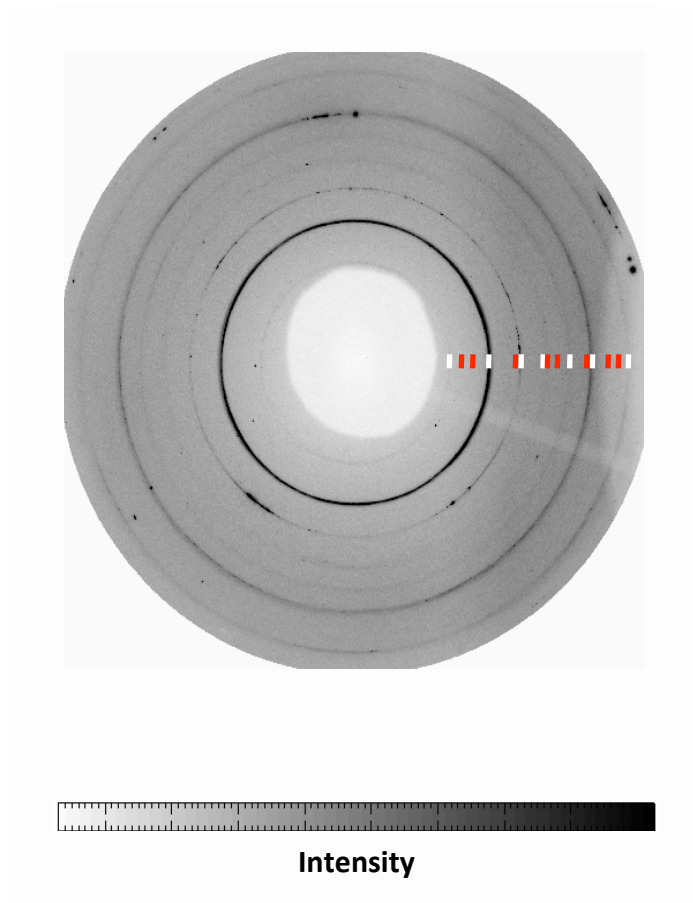
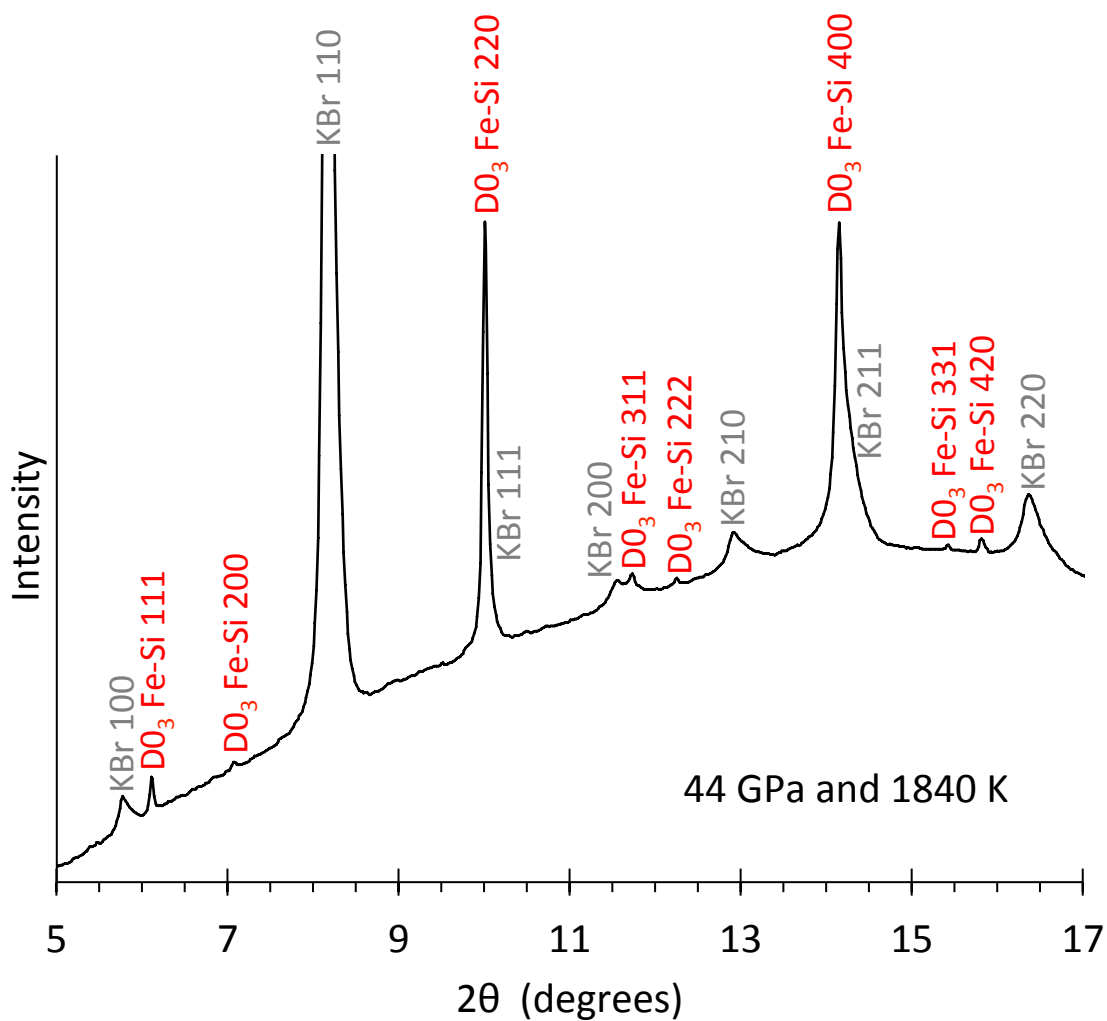


Figure 2

A



B



C

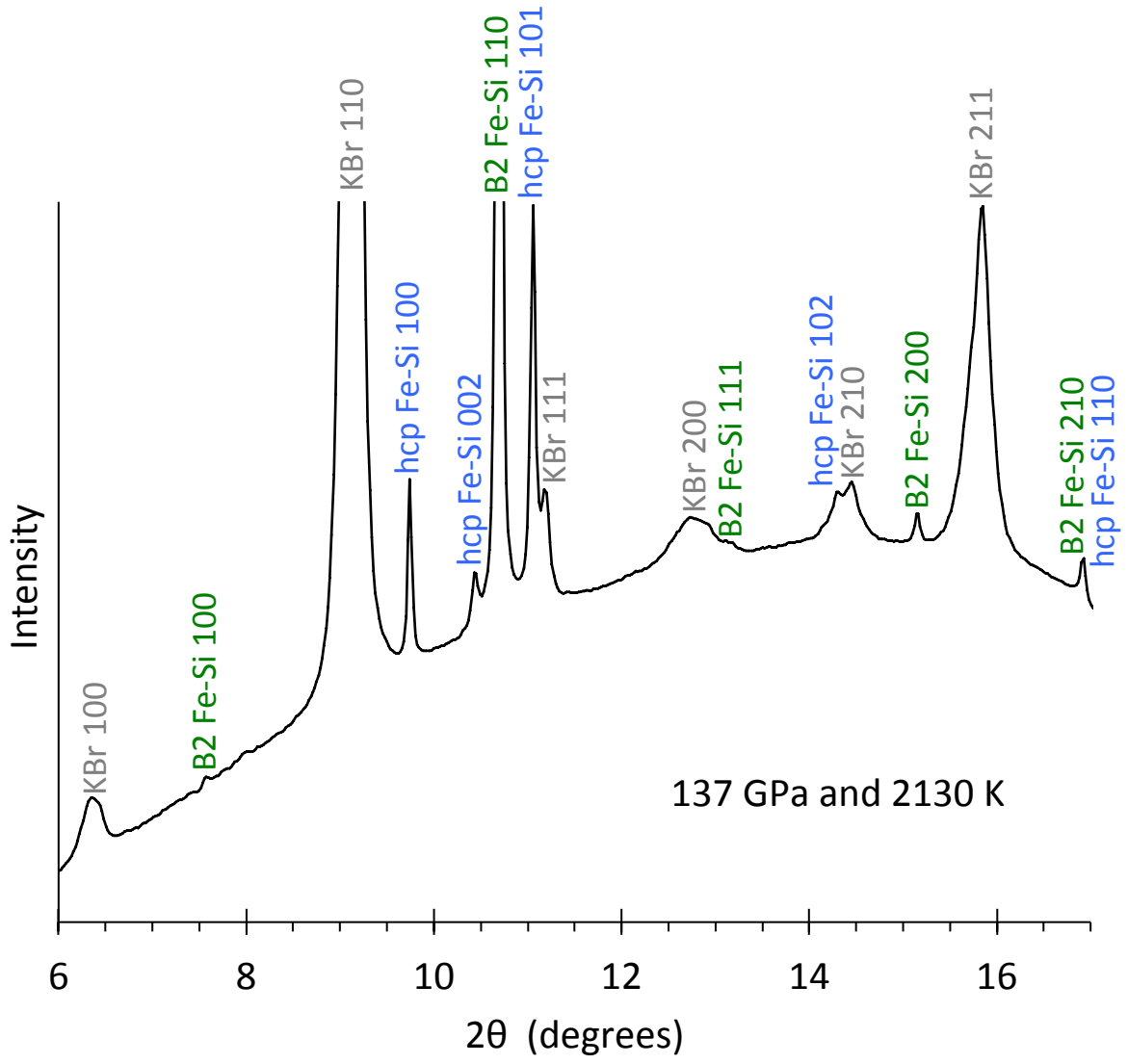


Figure 3

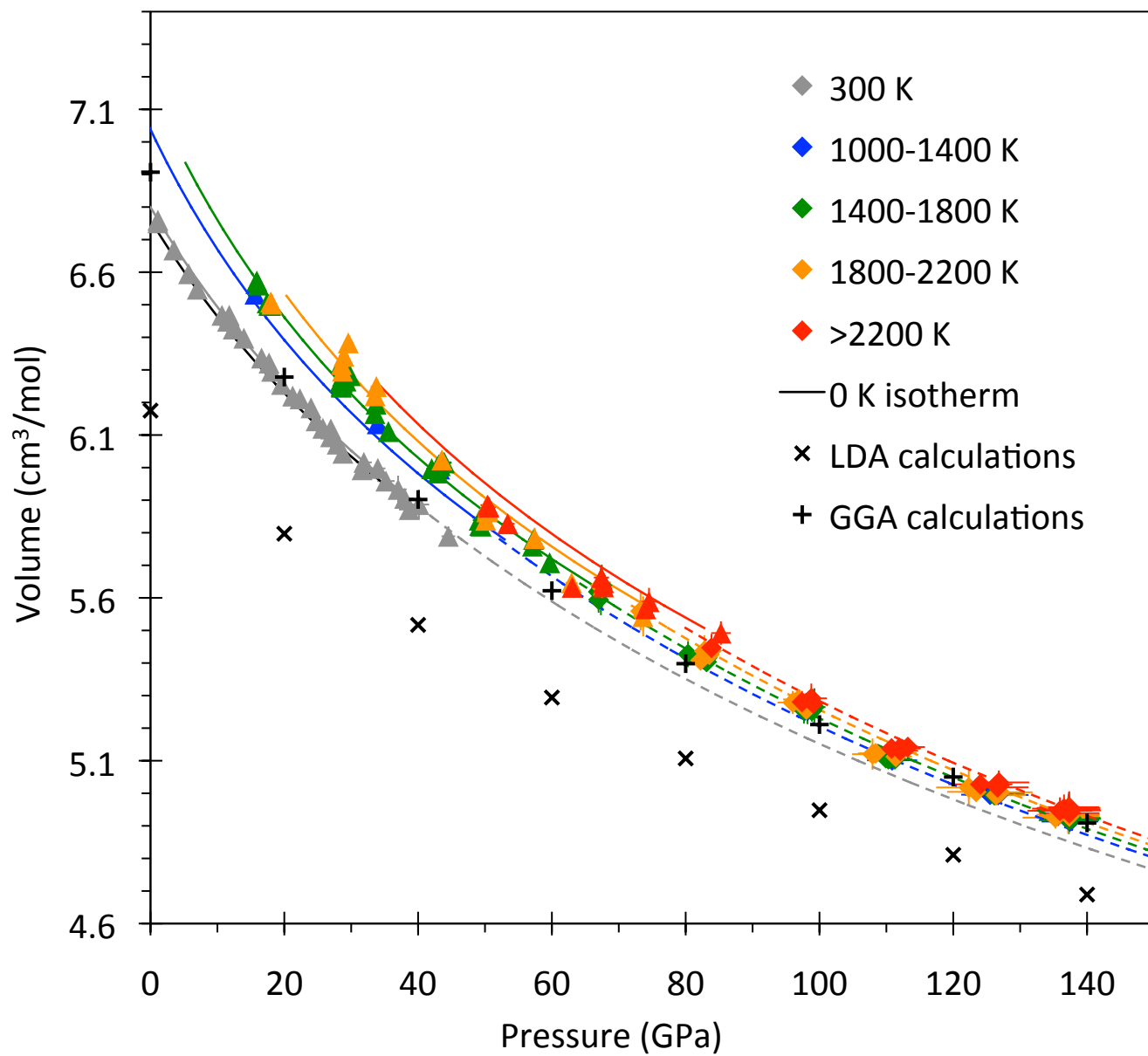


Figure 4

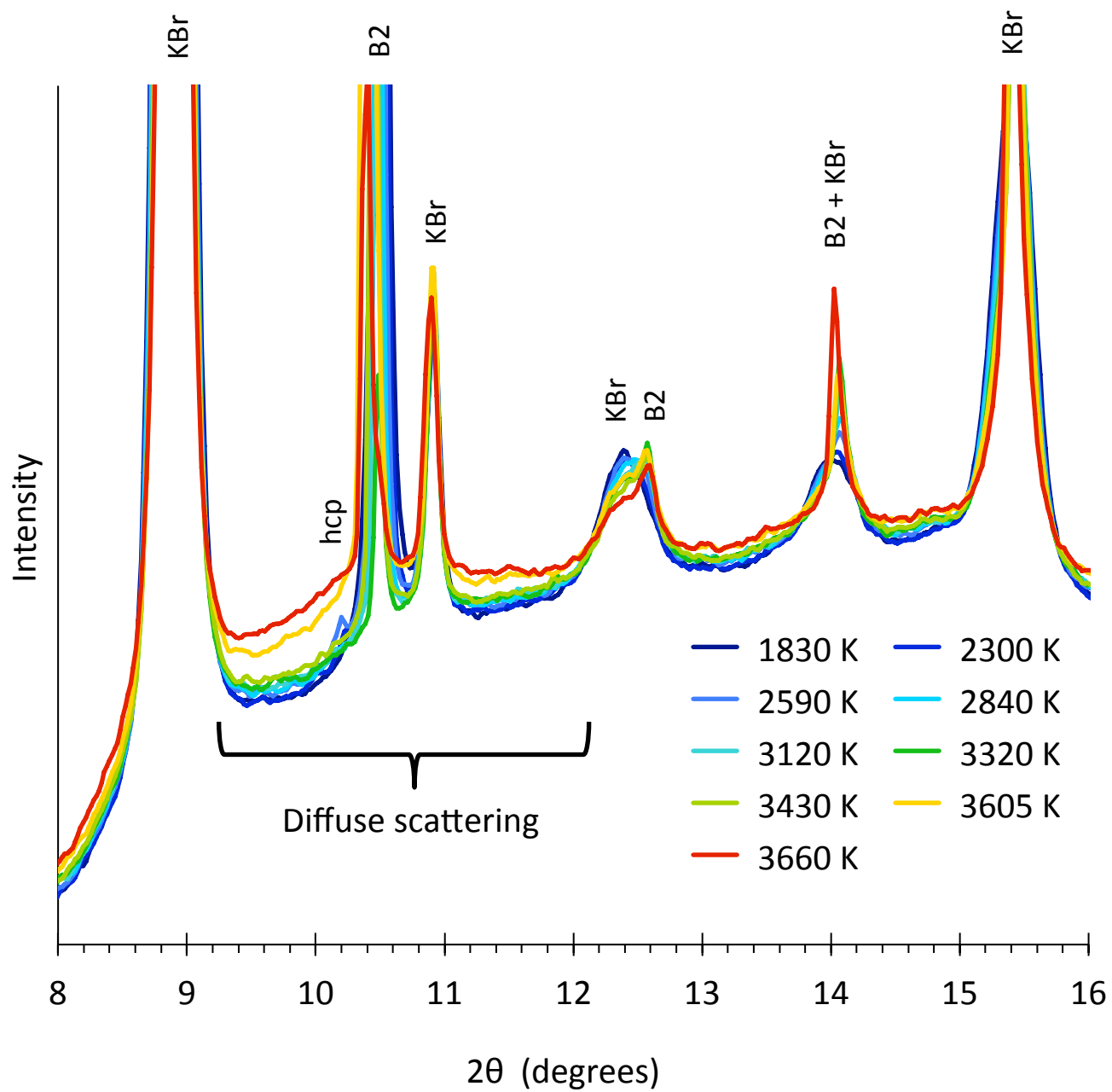


Figure 5

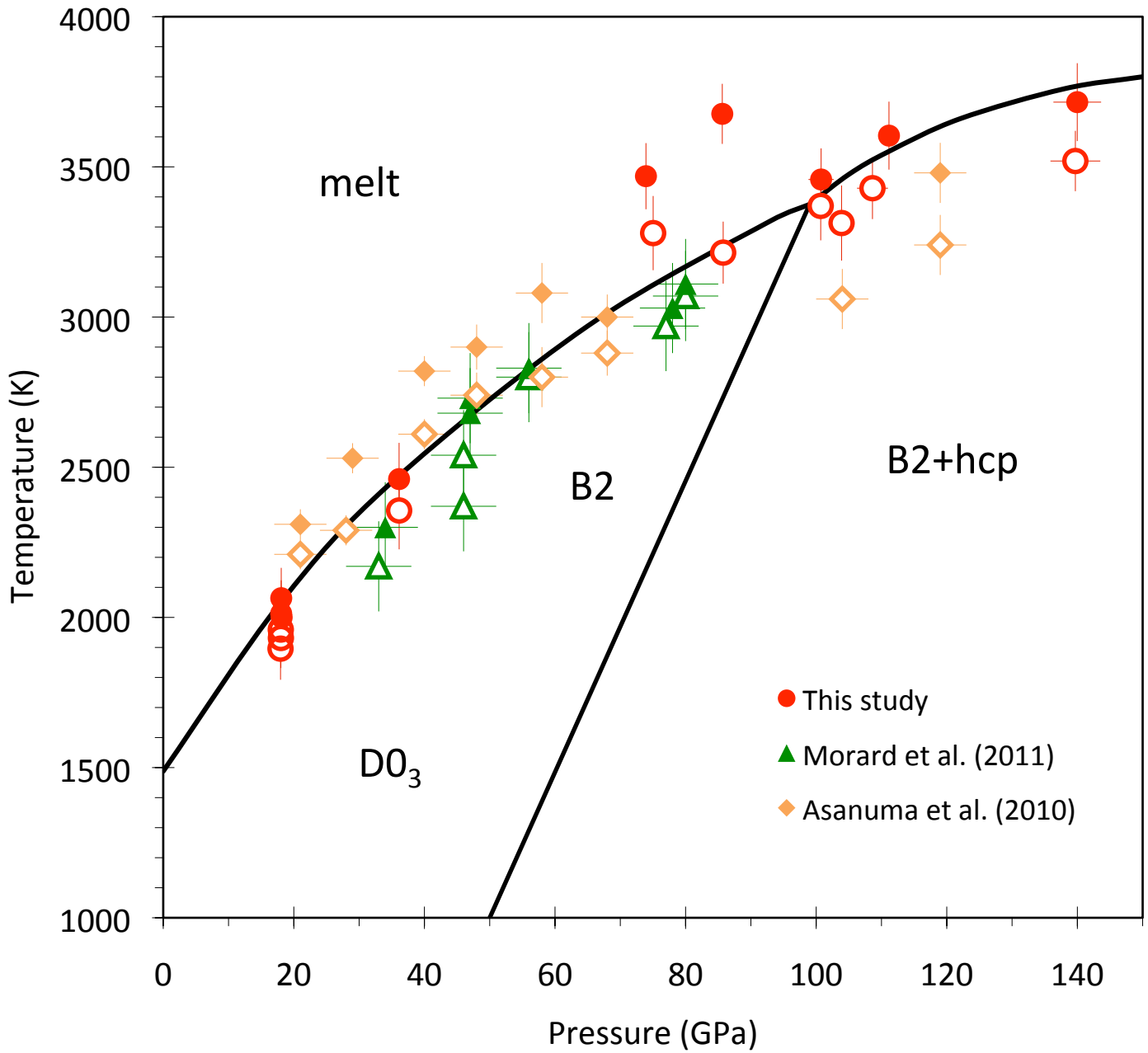
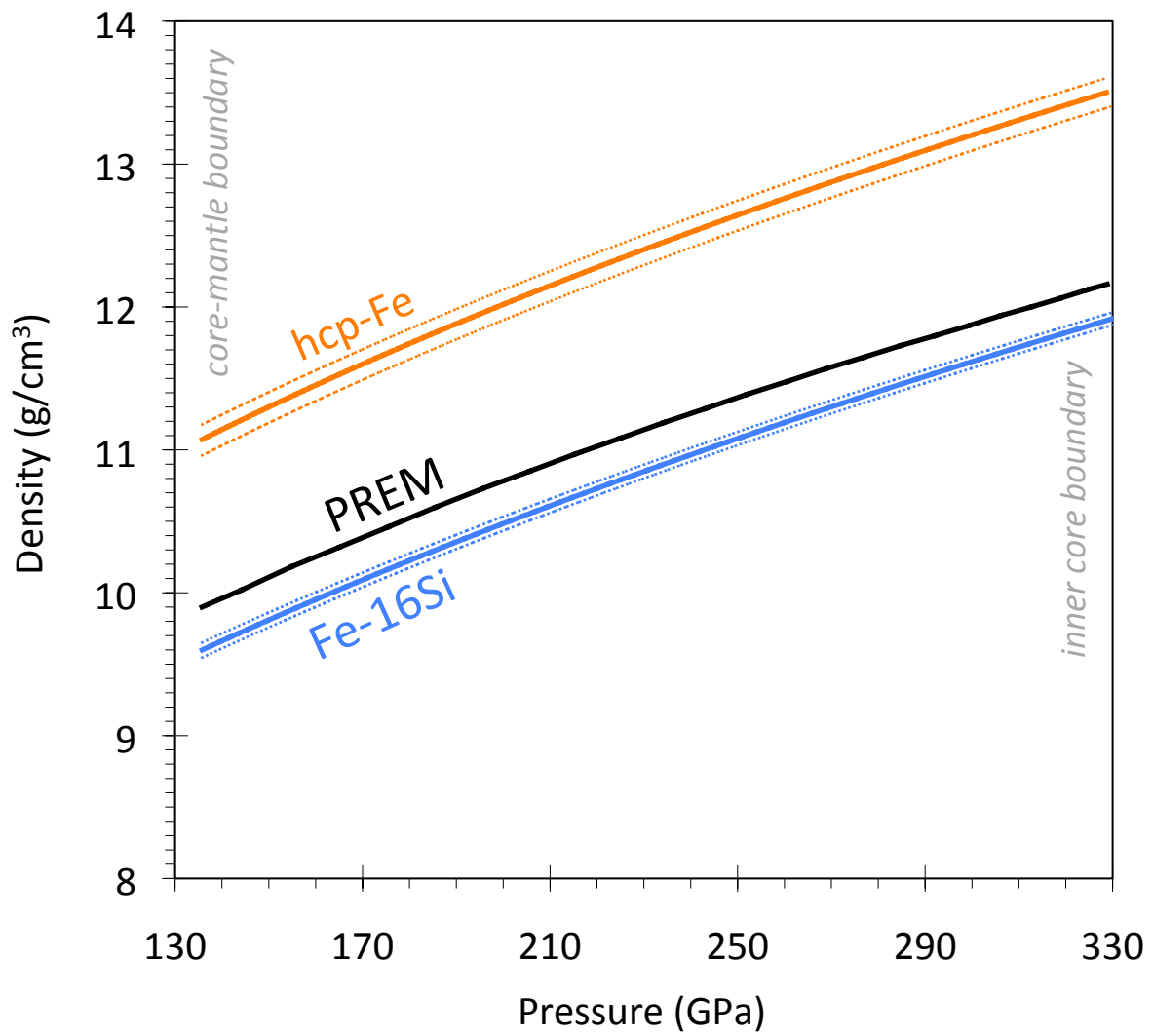


Figure 6



## **Supplemental Methods:**

### ***Correction to KBr lattice parameters:***

We performed a small correction to the measured lattice parameters of KBr at 300 K to account for deviatoric stresses (after Singh, 1993). We plotted the measured lattice parameter of KBr computed from each  $d$ -spacing versus the  $2\theta$  angle of that peak (Supplemental Figure S3), finding a linear trend, which indicates that the  $\theta$  dependence of the strain dominates over the  $hkl$  dependence, contrary to the results of Shim et al. (2000). Therefore, we then performed an unweighted linear fit to the data, taking the intercept (the extrapolation to  $2\theta=0$ ) as the lattice parameter, and the uncertainty in the intercept as the uncertainty in the lattice parameter. The average correction was a 0.08% decrease in KBr lattice parameter, which translated to 1.4% increase in pressure. The corrected and uncorrected KBr lattice parameters are shown as a function of the corrected pressure in Supplemental Figure S4. Performing the same analysis with the sample lattice parameters revealed no systematic relationship between strain and  $2\theta$  angle, so the measured sample lattice parameters were not corrected.

**Supplemental Figure S1:** A unit cell of the  $D0_3$  structure, generated using XtalDraw.

For Fe-16Si, green atoms represent sites mostly occupied by iron, and blue atoms represent sites mostly occupied by silicon.

**Supplemental Figure S2:** Magnetism of  $Fe_3Si$  in the  $D0_3$  crystal structure, calculated using LDA and GGA methods at 0 K.

**Supplemental Figure S3:** Uncorrected KBr lattice parameters determined from multiple  $d$ -spacings in a pattern collected at 11 GPa and 300 K, as a function of  $2\theta$  angle. The linear trend of the data reflects the dominance of the  $\theta$  dependence of the strain over any  $hkl$  effects, which may cause the scatter in the data. Since the  $\theta$  dependence dominates, we performed an unweighted linear fit (black line) and extrapolated to  $2\theta=0$  to find a corrected KBr lattice parameter of 3.617 Å.

**Supplemental Figure S4:** Corrected and uncorrected KBr lattice parameters as a function of pressure (calculated from the corrected lattice parameter) at room temperature.

**Supplemental Table S1:** Pressure-volume-temperature brackets on the hcp-fcc transition in pure iron, used to benchmark temperature measurements (Fischer et al., 2011). Measured volumes and temperatures are compared to those of Komabayashi and Fei (2010).

**Supplemental Table S2:** Pressure-volume-temperature data from synchrotron X-ray diffraction experiments.

**Supplemental Table S3:** Magnetism and volumes of Fe<sub>3</sub>Si in the D0<sub>3</sub> structure at 0 K calculated using LDA and GGA methods.

**Supplemental Table S4:** Pressures and temperatures of upper and lower bounds on melting from X-ray diffuse scattering.

**Supplemental Table S5:** Volumes of hcp iron at high pressures, calculated using GGA.

**Supplemental Table S6:** Volumes of B2-FeSi at high pressures, calculated using GGA.

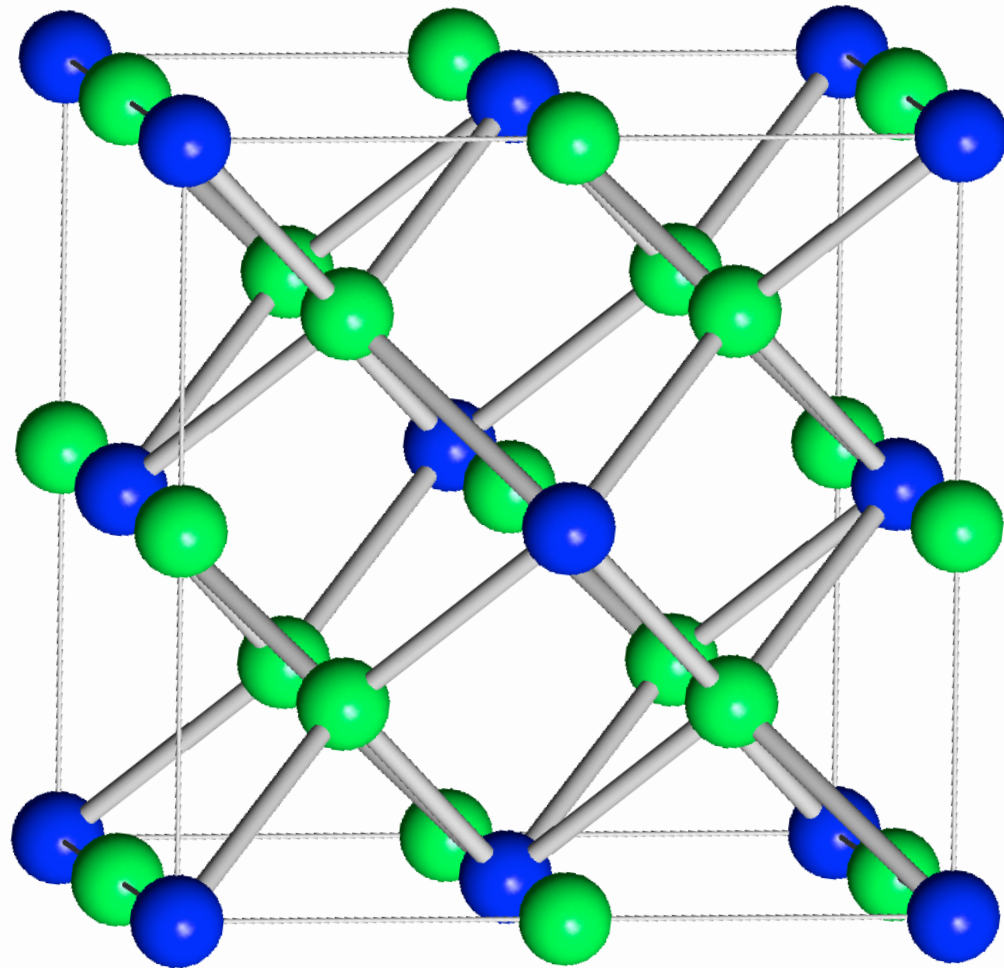
**References:**

- Campbell, A.J., Seagle, C.T., Heinz, D.L., Shen, G., Prakapenka, V.B., 2007. Partial melting in the iron-sulfur system at high pressure: A synchrotron X-ray diffraction study. *Phys. Earth Planet. Inter.* 162, 119-128.
- Campbell, A.J., Danielson, L., Richter, K., Seagle, C.T., Wang, Y., Prakapenka, V.B., 2009. High pressure effects on the iron-iron oxide and nickel-nickel oxide oxygen fugacity buffers. *Earth Planet. Sci. Lett.* 286, 556-564.
- Dewaele, A., Loubeyre, P., Occelli, F., Mezouar, M., Dorogokupets, P.I., Torrent, M., 2006. Quasihydrostatic equation of state of iron above 2 Mbar. *Phys. Rev. Lett.* 97, 215504.
- Fischer, R.A., Campbell, A.J., Shofner, G.A., Lord, O.T., Dera, P., Prakapenka, V.B., 2011. Equation of state and phase diagram of FeO. *Earth Planet. Sci. Lett.* 304, 496-502.
- Komabayashi, T., Fei, Y., 2010. Internally consistent thermodynamic database for iron to the Earth's core conditions. *J. Geophys. Res.* 115, B03202.

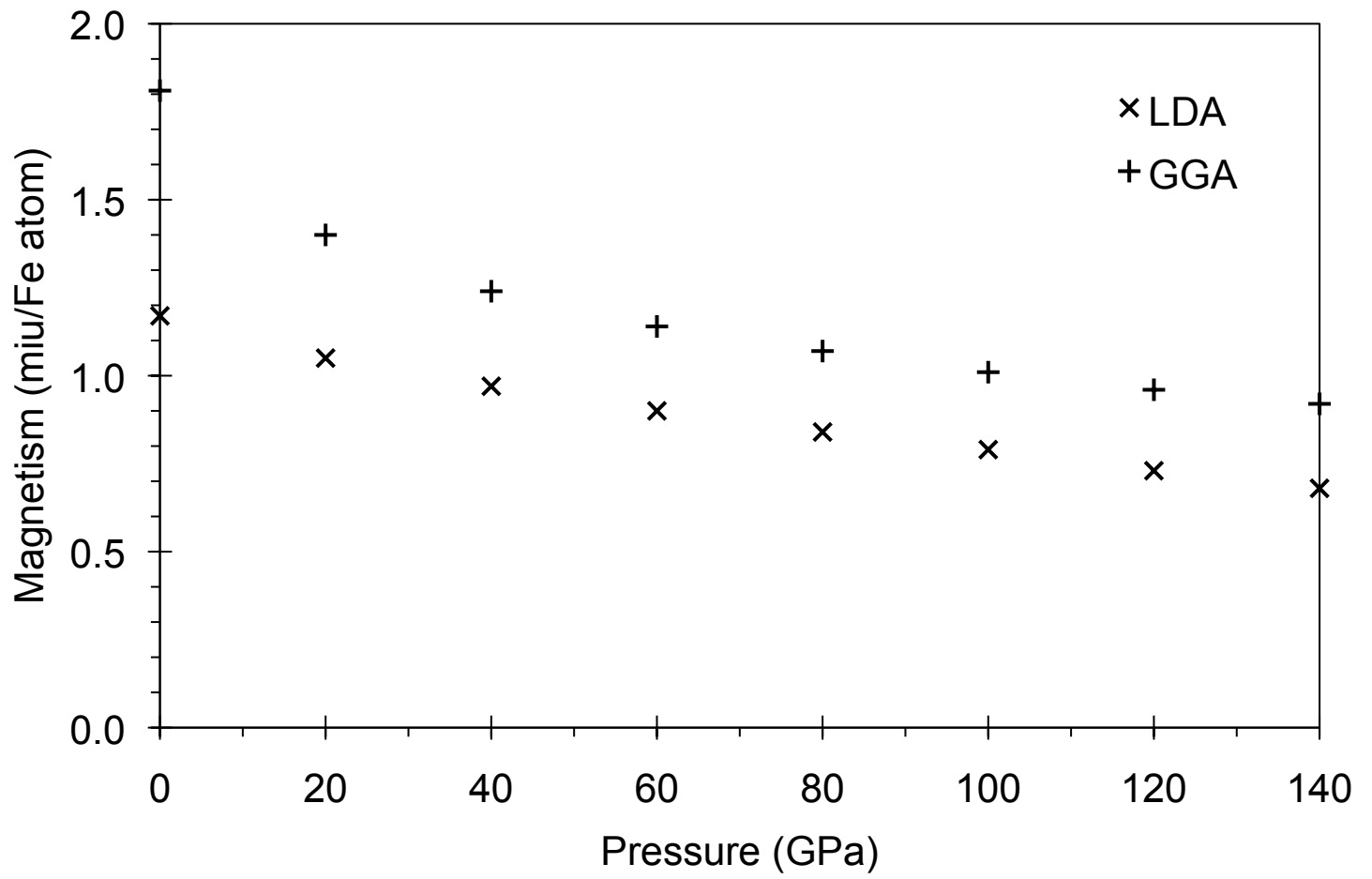
Shim, S.-H., Duffy, T.S., Shen, G., 2000. The equation of state of CaSiO<sub>3</sub> perovskite to 108 GPa at 300 K. *Phys. Earth Planet. Int.* 120, 327-338.

Singh, A.K., 1993. The lattice strains in a specimen (cubic system) compressed nonhydrostatically in an opposed anvil device. *J. Appl. Phys.* 73, 4278-4286.

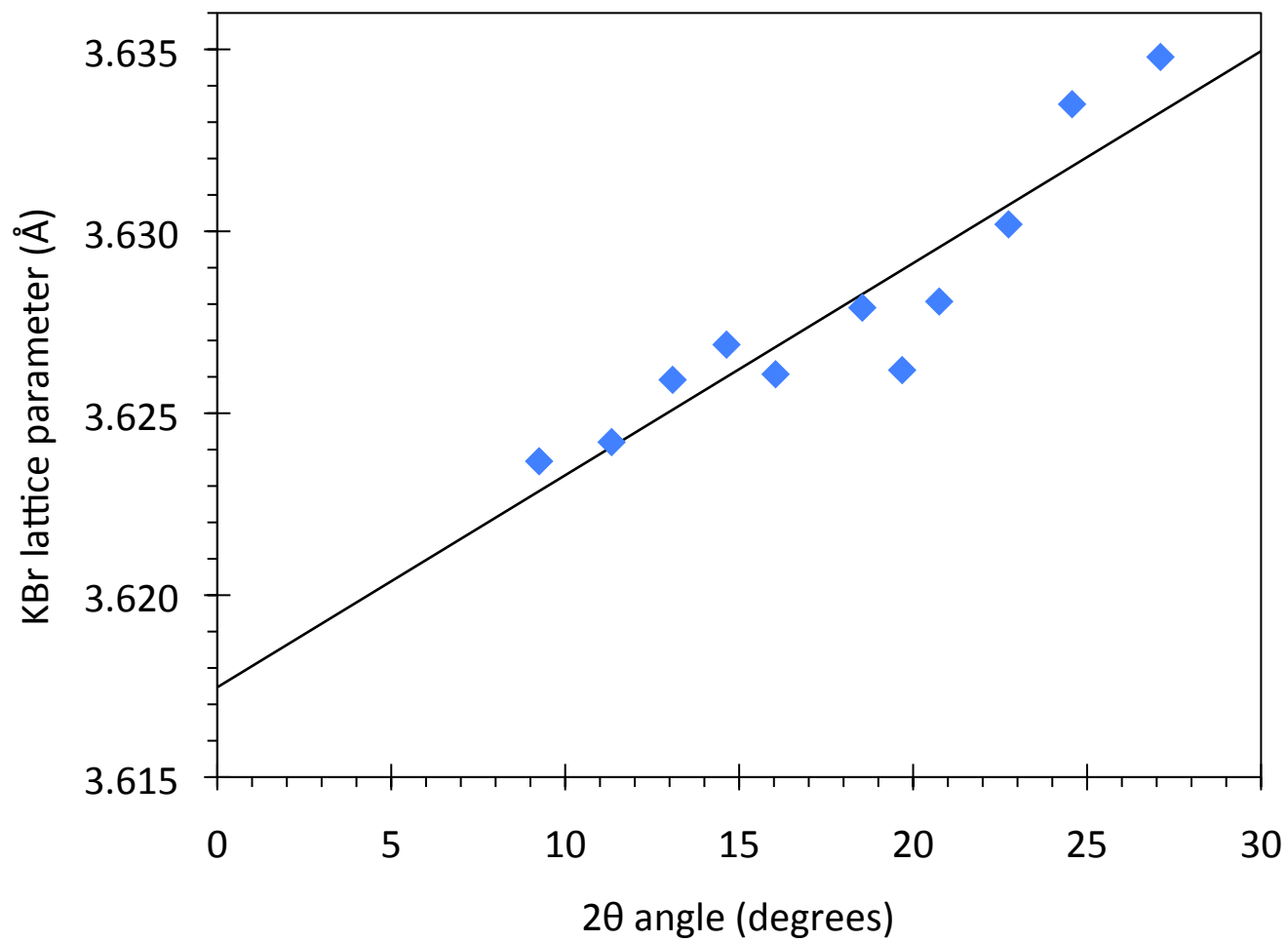
Supplemental Figure 1



Supplemental Figure 2



Supplemental Figure 3



Supplemental Figure 4

